Numerical simulation of non-viscous liquid pinch-off using a coupled level set-boundary integral method ☆

M. Garzon [a], L.J. Gray [d], J.A. Sethian [b,c,*]

[a] Department of Applied Mathematics, University of Oviedo, Spain
[b] Department of Mathematics, University of California, Berkeley, United States
[c] Mathematics Department, Lawrence Berkeley National Laboratory, United States
[d] Computer Science and Mathematics Division, Oak Ridge National Laboratory, United States

ARTICLE INFO

ABSTRACT

Simulations of the pinch-off of an inviscid fluid column are carried out based upon a potential flow model with capillary forces. The interface location and the time evolution of the free surface boundary condition are both approximated by means of level set techniques on a fixed domain. The interface velocity is obtained via a Galerkin boundary integral solution of the 3D axisymmetric Laplace equation. A short-time analytical solution of the Raleigh–Taylor instability in a liquid column is available, and this result is compared with our numerical experiments to validate the algorithm. The method is capable of handling pinch-off and after pinch-off events, and simulations showing the time evolution of the fluid tube are presented.

© 2009 Elsevier Inc. All rights reserved.

1. Introduction and overview

A significant challenge in the numerical solution of free boundary problems is when the domain undergoes topological changes. This is often the case for the potential flow models that describe a variety of important fluid flow problems, the Rayleigh–Taylor (or Rayleigh–Plateau) instability of a fluid column considered herein being a prime example [26,27]. A second critical aspect of these (and other) simulations is that, on the free surface, the boundary condition for the Laplace equation must be obtained by solving a separate partial differential equation defined on the evolving front.

The Level Set Method was specifically designed to cope with topological changes in moving boundary problems [35]. Moreover, for advancing material properties defined and governed by a differential equation on the front, effective Level Set techniques have been recently developed [3]. As the Level Set approach produces (almost directly) a new surface mesh if desired, it invites solving the governing equation in the volume by means of a Boundary Integral analysis. These combined methods were first applied to successfully simulate complex dendritic growth in solidification [30]. More recent work has investigated the field emission of liquid droplets [38] and interface motion in two phase flows [8]. The Level Set algorithm for advancing the free boundary condition was initially employed to model the propagation and breaking of waves over

sloping beaches [12,13]. In this work however, due to the limitation of the potential flow assumption, modeling of the wave after breaking (reconnection) was not attempted.

Drop formation problems, for viscous and non-viscous fluids, have been widely studied for many years due to its fascinating nature and interest in various technical and industrial fields, such as inkjet printing, sprays and electrosprays, etc. The first outstanding contributions were due to Savart [28], Plateau [26] and Rayleigh [27] and an extensive review of fluid break up has been given by Eggers [10,11]. Other interesting works in this field can be found in [4,6,18,21,24,29].

In this paper an inviscid fluid under the effect of capillary forces will be studied. Assuming that the liquid (*e.g.*, water) remains in the inviscid regime down to molecular scales, pinch-off and drop formation will result in a Rayleigh–Taylor instability. It has been shown theoretically [5,9] and computationally [19] that the phenomenon of inviscid pinch-off is asymptotically self-similar with both radial and axial length scales decreasing as $\tau^{2/3}$ and velocities increasing like $\tau^{-1/3}$, where τ is the time to pinch-off. It will be demonstrated that these results can be observed in the numerical simulations, validating the numerical methods.

A mathematical model and numerical approximation for the evolution of a 3D axisymmetric fluid domain is presented, capturing the time evolution of a fluid column before and after pinch-off events. The algorithm is capable of continuing the evolution of the first drops through the subsequent cascade of drop formation.

The paper is organized as follows: In Section 2 we present the model equations for an inviscid fluid flow in 3D and its axisymmetric version using a Lagrangian–Eulerian formulation. The complete Eulerian approach of the model equations using the Level Set Method is established in Section 3; we also demonstrate that the recasted system of PDE's automatically incorporates topological changes of the free surface and the evolution of the associated velocity potential function. In Section 4 we present the numerical schemes used, with a detailed description of the complete algorithm. Finally, in Section 5, we first present numerical results for the linearized model and compare them with the short-time analytical solution. Then, the full nonlinear approximation is used to compute the evolution of the fluid column before and after first pinch-off, following the satellite drop evolution and its subsequent break up. A series of numerical experiments are carried out to show the convergence of the algorithm. We complete the validation of the numerical results by checking the self-similar scaling laws for the first pinch-off, as well as the subsequent pinch-off occurrences.

2. The governing equations

To model the Rayleigh–Taylor problem, consider an infinite liquid column in the absence of gravity and initially at rest. Movement of the fluid is induced by perturbing the free surface of the cylinder with a small amplitude wave of wave number $k = \frac{2\pi}{L}$. For the numerical simulations, the domain will be made finite by introducing lateral boundaries for the cylinder and imposing periodic boundary conditions for these surfaces.

Let $\Omega(t)$ be the 3D cylindrical fluid domain surrounded by air and $\Gamma_t(\mathbf{s}) = (x(\mathbf{s}, t), y(\mathbf{s}, t), z(\mathbf{s}, t))$ a parametrization of the free surface boundary at time t (see Fig. 1). For an incompressible and inviscid fluid, the governing equations are the Euler equations

$$\nabla \cdot \mathbf{u} = 0 \quad \text{in } \Omega(t), \tag{1}$$

$$\mathbf{u}_t + \mathbf{u} \cdot (\nabla \cdot \mathbf{u}) = \frac{-\nabla p}{\rho} + \mathbf{b} \quad \text{in } \Omega(t), \tag{2}$$

where $\mathbf{u}(x, y, z, t)$ is the fluid velocity, $p(x, y, z, t)$ the pressure field, $\mathbf{b}(x, y, z, t)$ the body forces (per unit mass), and ρ is the fluid density.

Further, if irrotationality is assumed, the vorticity vanishes everywhere in the flow. In this case, the Helmholtz decomposition states that the velocity field can be represented as the gradient of a scalar function, referred to as the velocity potential $\phi(x, y, z, t)$. Thus, $\mathbf{u} = \nabla \phi$, and the Euler equations can be written as
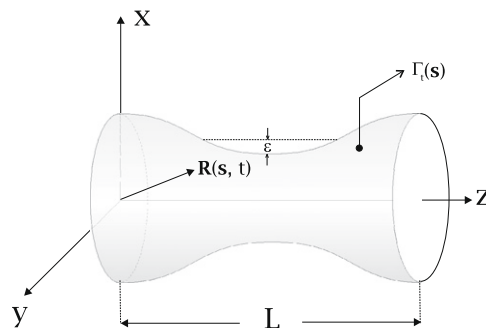

Fig. 1. Cylinder geometry in 3D.

$$\Delta\phi = 0 \quad \text{in } \Omega(t), \tag{3}$$

$$\phi_t + \frac{1}{2}(\nabla\phi \cdot \nabla\phi) + \frac{p - p_a}{\rho} = 0 \quad \text{in } \Omega(t). \tag{4}$$

Here p_a denotes the atmospheric pressure.

On the free boundary, the continuity of the stress tensor between water and air leads to the balance of the surface tension forces, $p = p_a + \gamma\left(\frac{1}{R_1} + \frac{1}{R_2}\right)$, where R_1 and R_2 are the principal radii of curvature of $\Gamma_t(\mathbf{s})$ and γ is the surface tension coefficient. Thus Eq. (4) becomes

$$\phi_t + \frac{1}{2}(\nabla\phi \cdot \nabla\phi) + \frac{\gamma}{\rho}\left(\frac{1}{R_1} + \frac{1}{R_2}\right) = 0 \quad \text{on } \Gamma_t(\mathbf{s}). \tag{5}$$

Finally, with $\mathbf{R}(\mathbf{s},t) = (X(\mathbf{s},t), Y(\mathbf{s},t), Z(\mathbf{s},t))$ the position vector of a fluid particle on the free surface, the kinematic boundary condition states

$$\mathbf{R}_t(\mathbf{s},t) = \mathbf{u}(\mathbf{R}(\mathbf{s},t),t) \quad \text{on } \Gamma_t(\mathbf{s}),$$

where $\mathbf{s} = (s_1, s_2)$ identifies the fluid particle that is at $x = X(\mathbf{s},t), y = Y(\mathbf{s},t), z = Z(\mathbf{s},t)$ at time t. The complete model equations in 3D are therefore

$$\mathbf{u} = \nabla\phi \quad \text{in } \Omega(t), \tag{6}$$

$$\Delta\phi = 0 \quad \text{in } \Omega(t), \tag{7}$$

$$\mathbf{R}_t = \mathbf{u} \quad \text{on } \Gamma_t(\mathbf{s}), \tag{8}$$

$$\frac{D\phi}{Dt} = \frac{1}{2}(\nabla\phi \cdot \nabla\phi) - \frac{\gamma}{\rho}\left(\frac{1}{R_1} + \frac{1}{R_2}\right) \quad \text{on } \Gamma_t(\mathbf{s}), \tag{9}$$

with the material derivative defined in the standard way

$$\frac{D}{Dt} = \frac{\partial}{\partial t} + \mathbf{u} \cdot \nabla.$$

If rotational symmetry around the z axis is now assumed, the free boundary is given by a curve in the (r,z) plane, i.e., $\Gamma_t(s)$ can be taken as the $x > 0$ section of the intersection of the three-dimensional boundary surface with the $y = 0$ plane. The velocity and the potential inside the fluid are denoted by $u(r,z,t)$ and $\phi(r,z,t)$, respectively and the two-dimensional problem can therefore be stated as

$$\mathbf{u} = \nabla\phi \quad \text{in } \Omega_d(t), \tag{10}$$

$$\frac{\partial^2\phi}{\partial r^2} + \frac{\partial^2\phi}{\partial z^2} + \frac{1}{r}\frac{\partial\phi}{\partial r} = 0 \quad \text{in } \Omega_d(t), \tag{11}$$

$$\mathbf{R}_t = \mathbf{u} \quad \text{on } \Gamma_t(s), \tag{12}$$

$$\frac{D\phi}{Dt} = \frac{1}{2}(\nabla\phi \cdot \nabla\phi) - \frac{\gamma}{\rho}\left(\frac{1}{R_1} + \frac{1}{R_2}\right) \quad \text{on } \Gamma_t(s). \tag{13}$$

Here $\Omega_d(t)$ denotes the fluid domain in two dimensions, and $\mathbf{R}(s,t) = (\text{R}(s,t), \text{z}(s,t))$ is the corresponding position vector of a fluid particle located at the free boundary, see Fig. 2.

2.1. Dimensionless formulation

For the numerical implementation, it is convenient to reformulate the above equations in dimensionless form. To this end, the characteristic length is chosen as the cylinder radius r_0. The characteristic time is taken as

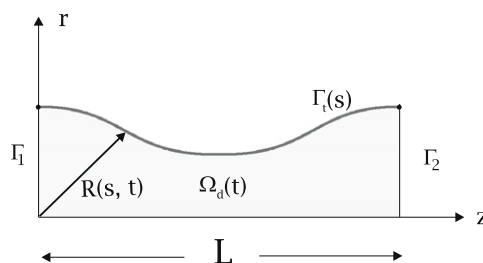$$t_0 = \left(\frac{\rho r_0^3}{\gamma}\right)^{\frac{1}{2}},$$

Fig. 2. Cylinder geometry in the r–z plane.

which comes from setting the ratio between inertial and surface tension forces equal to one. The dimensionless variables are then

$$\tilde{\phi}(\tilde{r}, \tilde{z}, \tilde{t}) = \frac{t_0}{r_0^2} \phi(r, z, t), \quad \tilde{r} = \frac{r}{r_0}, \quad \tilde{z} = \frac{z}{r_0}, \quad \tilde{t} = \frac{t}{t_0}, \quad \tilde{u} = \frac{t_0}{r_0} u, \tag{14}$$

and Eq. (13) for the free surface boundary condition becomes

$$\frac{D\tilde{\phi}}{D\tilde{t}} = \frac{D\tilde{\phi}}{Dt} \frac{Dt}{D\tilde{t}} = \frac{t_0^2}{r_0^2} \frac{D\phi}{Dt} = \frac{t_0^2}{r_0^2} \left(\frac{1}{2} (\nabla \phi \cdot \nabla \phi) - \frac{\gamma}{\rho} \left(\frac{1}{R_1} + \frac{1}{R_2} \right) \right) = \frac{1}{2} \left(\nabla \tilde{\phi} \cdot \nabla \tilde{\phi} \right) - \left(\frac{1}{\tilde{R_1}} + \frac{1}{\tilde{R_2}} \right). \tag{15}$$

In what follows, the tilde designating the dimensionless variables will be dropped, and the dimensionless model can then be written as

$$\mathbf{u} = \nabla \phi \quad \text{in } \Omega_d(t), \tag{16}$$

$$\frac{\partial^2 \phi}{\partial r^2} + \frac{\partial^2 \phi}{\partial z^2} + \frac{1}{r} \frac{\partial \phi}{\partial r} = 0 \quad \text{in } \Omega_d(t), \tag{17}$$

$$\mathbf{R}_t = \mathbf{u} \quad \text{on } \Gamma_t(s), \tag{18}$$

$$\frac{D\phi}{Dt} = \frac{1}{2} (\nabla \phi \cdot \nabla \phi) - \left(\frac{1}{R_1} + \frac{1}{R_2} \right) \quad \text{on } \Gamma_t(s). \tag{19}$$

To simplify notation further, Eq. (17) will be written as $\Delta \phi(r, z) = 0$. Eqs. (16)–(19) are the Lagrangian–Eulerian formulation of the fluid motion. In classical front tracking methods for this system of partial differential equations, a fixed number of fluid particles are chosen at the initial time and the trajectories of these particles are followed as time evolves. This method suffers difficulties when the free boundary changes topology, and thus the next section develops an approach based upon a Level Set formulation.

3. Level Set framework

Level set [25] methods represent a propagating surface as the zero level set of a time-dependent, implicit function, and then solve the resulting equations of motion for this function in a fixed grid Eulerian setting. They rely in part on the theory of curve and surface evolution given in [31,32] and on the link between front propagation and hyperbolic conservation laws discussed in [33]. Physically appropriate viscosity solutions are obtained by exploiting schemes from the numerical solution of hyperbolic conservation laws. Level set methods are designed for problems involving topological change, curvature dependence, geometric singularities (*i.e.*, cusps), and complex three-dimensional problems. These methods were made efficient using the Narrow Band Level Set Method strategy developed by Adalsteinsson and Sethian in [1]. For further information, see the monograph by Sethian [35], as well as the review in [36]; applications to bubble and jets may be found in [40].

Briefly, the main idea is to embed the initial position of the front as the zero level set of the higher-dimensional function $\Psi(r, z, t)$. The evolution of this function Ψ is linked to the propagation of the actual front through a time-dependent initial value problem. In this manner, the front at any given time is the zero level set of Ψ. An equation of motion for Ψ that ties the zero level set of Ψ to the evolving front comes from observing that the level set value of a particle on the front with path $\mathbf{R}(s, t)$ must always be zero:

$$\Psi(\mathbf{R}(s, t), t) = 0.$$

Hence by the chain rule, we have that

$$\Psi_t + \nabla \Psi(\mathbf{R}(s, t), t) \cdot \mathbf{u} = 0. \tag{20}$$

For the Rayleigh–Taylor problem, let Ω_D be a fictitious fixed rectangular domain that contains the free boundary at any time t. Eq. (18), which states that the front moves with velocity $\mathbf{u}$, can be replaced by the level set equation (20) posed on Ω_D.

To embed the free surface boundary condition given by Eq. (19) into the level set framework, the curve that represents the initial position of the front is parametrized by its arclength: $s \to \Gamma_0(s)$. For the velocity field $\mathbf{u}(r, z, t)$, the trajectory of a fluid particle at initial position s is given by the solution of

$$\mathbf{R}_t(s, t) = \mathbf{u}(\mathbf{R}(s, t), t),$$
$$\mathbf{R}(s, 0) = (\text{R}(s, 0), \text{Z}(s, 0)). \tag{21}$$

For $t > 0$ the free boundary curves are parametrized with the same parameter $s, s \to \Gamma_t(s)$, in order to have the identity $\Gamma_t(s) := \mathbf{R}(s, t)$.

On the free boundary $\Gamma_t(s)$ define

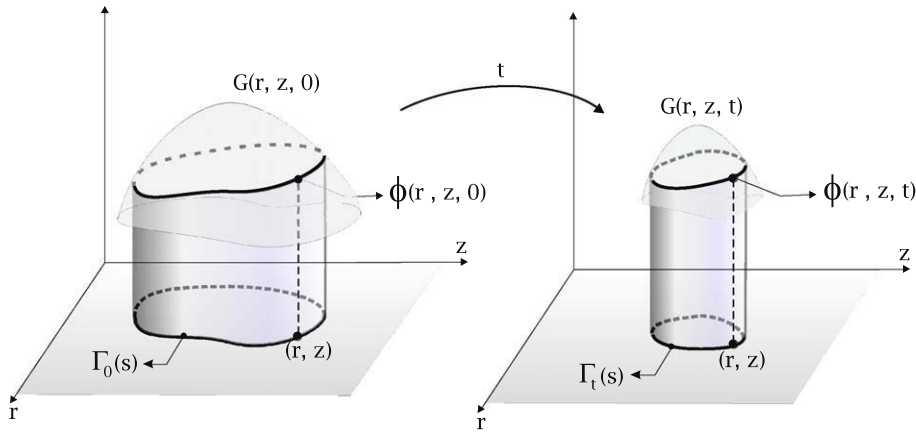$$\Phi(s, t) = \phi(r, z, t)|_{\Gamma_t(s)} = \phi(\mathbf{R}(s, t), t),$$

Fig. 3. Extension of the velocity potential off the front.

so that by fixing s and moving t, we are constrained to a fluid particle. As a consequence, $\Phi_t(s,t)$ is a total derivative and hence

$$\Phi_t = \phi_t + \mathbf{u} \cdot \nabla\phi = \frac{1}{2}(\nabla\phi \cdot \nabla\phi) - \left(\frac{1}{R_1} + \frac{1}{R_2}\right).$$

Next, let $G(r,z,t)$ be a function defined on Ω_D such that on $\Gamma_t(s)$

$$G(\mathbf{R}(s,t), \mathbf{z}(s,t), t) = \Phi(s,t). \tag{22}$$

It is important to remark here that $G(r,z,t)$ is an auxiliary function that can be chosen arbitrarily, with the only restriction that it is equal to $\phi(r,z,t)$ on $\Gamma_t(s)$ (see Fig. 3).

Applying the chain rule in the identity (22) we obtain

$$G_t + \mathbf{u} \cdot \nabla G = \frac{1}{2}(\nabla\phi \cdot \nabla\phi) - \left(\frac{1}{R_1} + \frac{1}{R_2}\right), \tag{23}$$

which holds on $\Gamma_t(s)$. Note that $\mathbf{u}$ and the right-hand-side of Eq. (23) are only defined on $\Gamma_t(s)$, and thus, in order to solve Eq. (23) over the domain Ω_D, these variables must be extended off the front. That is, one must give meaning to both the velocity and the right-hand-side at points off of the interface in order to advance the level set function as well as this extended potential. This strategy will be discussed in Section 4, but for now assuming this extension, the system of equations, written in a complete Eulerian framework, is

$$\mathbf{u} = \nabla\phi \quad \text{in } \Omega_d(t), \tag{24}$$

$$\Delta\phi(r,z) = 0 \quad \text{in } \Omega_d(t), \tag{25}$$

$$\Psi_t + \mathbf{u}_{\text{ext}} \cdot \nabla\Psi = 0 \quad \text{in } \Omega_D, \tag{26}$$

$$G_t + \mathbf{u}_{\text{ext}} \cdot \nabla G = f_{\text{ext}} \quad \text{in } \Omega_D. \tag{27}$$

Here $f = \frac{1}{2}(\nabla\phi \cdot \nabla\phi) - \kappa, \kappa = R_1^{-1} + R_2^{-2}$ and the subscript "ext" denotes the extension of f and $\mathbf{u}$ onto Ω_D.

The free surface equations (18) and (19) have now been embedded into the higher dimension equations (26) and (27). Next it will be shown that the system (24)–(27) in fact enriches the kinematics of the system, in the sense that it can incorporate topological changes of the free surface, and as well the evolution of the associated potential function within this boundary.

3.1. Splitting of the fluid domain

Assume that, due to the underlying physics of the problem, the domain $\Omega_d(t)$ splits into two disjoint closed subdomains at $t = t_0$. As the air pressure p_a is assumed constant, the two fluid subdomains will necessarily evolve independently for $t > t_0$. It is therefore possible to write the Lagrangian–Eulerian formulation for each separate fluid subdomain $\Omega_1(t)$, $\Omega_2(t)$ with respectively moving boundaries $\Gamma_{t,1}(s)$ and $\Gamma_{t,2}(s)$,

$$\mathbf{u}_1 = \nabla\phi_1 \quad \text{in } \Omega_1(t), \tag{28}$$

$$\Delta\phi_1 = 0 \quad \text{in } \Omega_1(t), \tag{29}$$

$$(\mathbf{R}_1)_t = \mathbf{u}_1 \quad \text{on } \Gamma_{t,1}(s), \tag{30}$$

$$\frac{D\phi_1}{Dt} = \frac{1}{2}(\nabla\phi_1 \cdot \nabla\phi_1) - \kappa_1 \quad \text{on } \Gamma_{t,1}(s), \tag{31}$$

and

$$\mathbf{u}_2 = \nabla\phi_2 \quad \text{in } \Omega_2(t), \tag{32}$$

$$\Delta\phi_2 = 0 \quad \text{in } \Omega_2(t), \tag{33}$$

$$(\mathbf{R}_2)_t = \mathbf{u}_2 \quad \text{on } \Gamma_{t,2}(s), \tag{34}$$

$$\frac{D\phi_2}{Dt} = \frac{1}{2}(\nabla\phi_2 \cdot \nabla\phi_2) - \kappa_2 \quad \text{on } \Gamma_{t,2}(s). \tag{35}$$

For $t > t_0$, each of the free boundary curves are parametrized as before with the parameter s, $s \to \Gamma_{t,1}(s)$, $s \to \Gamma_{t,2}(s)$, in order to have the identities $\Gamma_{t,1}(s) := \mathbf{R}_1(s,t)$ and $\Gamma_{t,2}(s) := \mathbf{R}_2(s,t)$.

On each free boundary

$$\Phi_1(s,t) = \phi_1(r,z,t)|_{\Gamma_{t,1}(s)} = \phi_1(\mathbf{R}_1(s,t),t),$$

$$\Phi_2(s,t) = \phi_2(r,z,t)|_{\Gamma_{t,2}(s)} = \phi_2(\mathbf{R}_2(s,t),t),$$

and hence

$$(\Phi_1)_t = \frac{1}{2}(\nabla\phi_1 \cdot \nabla\phi_1) - \kappa_1,$$

$$(\Phi_2)_t = \frac{1}{2}(\nabla\phi_2 \cdot \nabla\phi_2) - \kappa_2.$$

The extension function $G(r,z,t)$ defined on Ω_D is now constrained by the conditions

$$G(\mathrm{R}_1(s,t),\mathrm{Z}_1(s,t),t) = \Phi_1(s,t) \quad \text{on } \Gamma_{t,1}(s)$$

and

$$G(\mathrm{R}_2(s,t),\mathrm{Z}_2(s,t),t) = \Phi_2(s,t) \quad \text{on } \Gamma_{t,2}(s).$$

Applying the chain rule, G satisfies

$$G_t + \mathbf{u}_1 \cdot \nabla G = \frac{1}{2}(\nabla\phi_1 \cdot \nabla\phi_1) - \kappa_1 \quad \text{on } \Gamma_{t,1}(s), \tag{36}$$

$$G_t + \mathbf{u}_2 \cdot \nabla G = \frac{1}{2}(\nabla\phi_2 \cdot \nabla\phi_2) - \kappa_2 \quad \text{on } \Gamma_{t,2}(s). \tag{37}$$

Denote the right-hand sides in the free surface boundary conditions by $f_1 = \frac{1}{2}(\nabla\phi_1 \cdot \nabla\phi_1) - \kappa_1$ and $f_2 = \frac{1}{2}(\nabla\phi_2 \cdot \nabla\phi_2) - \kappa_2$. If the extensions $\mathbf{u}_{\text{ext}}$ and f_{ext} are defined in Ω_D so that $\mathbf{u}_{\text{ext}}|_{\Gamma_{t,1}(s)} = \mathbf{u}_1$, $\mathbf{u}_{\text{ext}}|_{\Gamma_{t,2}(s)} = \mathbf{u}_2$, $f_{\text{ext}}|_{\Gamma_{t,1}(s)} = f_1$ and $f_{\text{ext}}|_{\Gamma_{t,2}(s)} = f_2$, then

$$G_t + \mathbf{u}_{\text{ext}} \cdot \nabla G = f_{\text{ext}} \quad \text{in } \Omega_D$$

will automatically yield (36) and (37).

4. Numerical approximation of the Eulerian potential flow model

In this section and the next, brief overviews of the main components of the algorithm are provided. More detailed discussions of level set methods, boundary element methods, and fast extension velocities may be found in the cited references.

The numerical approximation of the coupled system of PDEs, (24)–(27), can be described in two basic steps. First, using a standard first order forward Euler explicit scheme to approximate time derivatives in the level set equations, the system to be solved for each time t_n and time step Δt is:

$$\mathbf{u^n} = \nabla\phi^n \quad \text{in } \Omega_d(t_n), \tag{38}$$

$$\Delta\phi^n(r,z) = 0 \quad \text{in } \Omega_d(t_n), \tag{39}$$

$$\frac{\Psi^{n+1} - \Psi^n}{\Delta t} = -\mathbf{u^n_{\text{ext}}} \cdot \nabla\Psi^n \quad \text{in } \Omega_D, \tag{40}$$

$$\frac{G^{n+1} - G^n}{\Delta t} = -\mathbf{u^n_{\text{ext}}} \cdot \nabla G^n + f^n_{\text{ext}} \quad \text{in } \Omega_D. \tag{41}$$

The second main task is to solve Eq. (39) for the free surface velocity, subject to the boundary condition $\phi^n = G^n$. This is accomplished by solving the boundary integral equation corresponding to the Laplace equation in the axisymmetric geometry depicted in Fig. 2, with the periodic boundary conditions,

$$\phi^n|_{\Gamma_1} = \phi^n|_{\Gamma_2}$$

$$\left.\frac{\partial\phi^n}{\partial\mathbf{n}}\right|_{\Gamma_1} = -\left.\frac{\partial\phi^n}{\partial\mathbf{n}}\right|_{\Gamma_2},$$

the details to be discussed in Section 4.3. With the computed velocity, the new position of the boundary is determined from the level set equation (40), and the potential on $\Gamma_{t_{n+1}}(s)$ will be obtained from Eq. (41). These procedures are described below.

4.1. Initialization

To initialize the system (38)–(41) the initial front position $\Gamma_0(s)$ and velocity potential $\phi(r, z, 0)$ are needed. We use the Rayleigh analytical solution given in [27]. Briefly it is obtained by considering a small perturbation ϵ of the cylinder free boundary and assuming that the potential function will be also small, that is:

$$r = 1 + \eta(z, t); \quad \eta = \epsilon\tilde{\eta}(z, t); \quad \phi(r, z, t) = \epsilon\tilde{\phi}(r, z, t). \qquad (42)$$

Inserting (42) into the full nonlinear model, Eqs. (16)–(19), and retaining first order terms in ϵ the linearized model obtained is:

$$\Delta\tilde{\phi} = 0,$$
$$\tilde{\eta}_t = \tilde{\phi}_r|_{r=1},$$
$$\tilde{\phi}_t = \tilde{\eta} + \tilde{\eta}_{zz}|_{r=1}.$$

Now, looking for solutions of the form

$$\tilde{\eta} = A(t)\cos(kz), \quad \tilde{\phi} = B(t)f(r)\cos(kz), \quad A(0) = 1, \quad B(0) = 0,$$

the analytical solution found is:

$$\phi(r, z, t) = \epsilon B(t) I_0(kr)\cos(kz),$$
$$\eta(z, t) = \epsilon A(t)\cos(kz),$$
$$A(t) = \cosh(\omega t),$$
$$B(t) = \frac{\omega}{k I_1(kr)}\sinh(\omega t),$$
$$\omega^2 = \frac{k I_1(k)}{I_0(k)}(1 - k^2),$$

which is valid for short times. Here $k = \frac{2\pi}{L}$ and L are the wave number and wave length of the perturbation. It is well known that the maximum growth rate corresponds to $k = 0.697$, see for example [10,27].

4.2. Level set numerical schemes

The fixed computational domain for Eqs. (40) and (41) is taken as $\Omega_D = [0, L_1] \times [0, L_2]$, L_2 being the length of the initial wave perturbation and L_1 such that Ω_D will contain the free boundary for all $t \in [0, T]$ (see Fig. 4).

A rectangular mesh over the domain Ω_D defines a set of points $D_\Delta = \{(r_i, z_j) : r_i = i\Delta r, z_j = j\Delta z, i = 1, N, j = 1, M\}$, with N, M the number of mesh points in the r and z directions and $\Delta r, \Delta z$ the corresponding mesh sizes. Let $\mathbf{n} = (n_r, n_z)$ be the unit normal vector to $\Gamma_{t_n}(s)$ and u, v the radial and axial velocity components. The axisymmetric assumption implies $u = 0$ and $n_r = 0$ at Γ_z. Moreover, due to the underlying physics of the problem the solution is not only periodic but also symmetric at $z = 0$ and $z = L_2$. These facts will be used to impose boundary conditions for (40) and (41),

$$v = 0 \quad \text{at } z = 0 \quad \text{and} \quad z = L_2,$$
$$\frac{\partial \Psi^n}{\partial r} = 0; \quad \frac{\partial G^n}{\partial r} = 0 \quad \text{at } \Gamma_z.$$

Let $G_{i,j}^n$ be the numerical approximation of the fictitious velocity potential $G(r_i, z_j, t_n)$. A first order upwind scheme approximation of Eq. (41) yields, for $i = 2, N-1$; $j = 2, M-1$,

$$G_{i,j}^{n+1} = G_{i,j}^n - \Delta t(\max(u_{i,j}^n, 0)D_{i,j}^{-r} + \min(u_{i,j}^n, 0)D_{i,j}^{+r} + \max(v_{i,j}^n, 0)D_{i,j}^{-z} + \min(v_{i,j}^n, 0)D_{i,j}^{+z}) + \Delta t f_{i,j}^n,$$
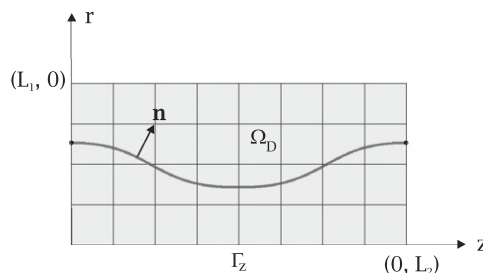

Fig. 4. Computational domain in the r–z plane.

where

$$D_{i,j}^{-r} = D_{i,j}^{-r}\left\{G_{i,j}^n\right\} = \frac{G_{i,j}^n - G_{i-1,j}^n}{\Delta r},$$

$$D_{i,j}^{+r} = D_{i,j}^{+r}\left\{G_{i,j}^n\right\} = \frac{G_{i+1,j}^n - G_{i,j}^n}{\Delta r}$$

are the backward and forward finite difference approximations for the derivative in the radial direction (the same expressions hold for the corresponding z derivatives $D_{i,j}^{-z}$ and $D_{i,j}^{+z}$). The discrete boundary conditions are:

$$v_{i,1} = 0 \quad \text{and} \quad v_{i,M} = 0 \quad \text{for } i = 1, N,$$

$$\frac{\partial G_{i,j}^n}{\partial r} \approx \frac{4G_{2,j}^n - 3G_{1,j}^n - G_{3,j}^n}{2\Delta r} \quad \text{for } (r_i, z_j) \in \Gamma_z,$$

$$G_{N,j}^n = G_{N-1,j}^n; \quad G_{1,j}^n = G_{2,j}^n \quad \text{for } j = 1, M.$$

The same discrete equations, without source term, can be written for Ψ, Eq. (40).

Note that, for simplicity, we have written u, v, f instead of $u_{\text{ext}}, v_{\text{ext}}, f_{\text{ext}}$, and we describe a first order explicit scheme with a centered source term. Initial values of $G_{i,j}^0$ are obtained by extending $\phi(r, z, 0)|_{\Gamma_0(s)}$. However, at any time step n it is always possible to perform a new extension of $\phi^n(r, z, n\Delta t)$ and a reinitialization of the level set function. We remark here that if reinitialization is done too often, especially using poor reinitialization techniques, spurious mass loss/gain will occur. Thus, it is important to perform reinitialization both sparingly and accurately.

A key issue is how one obtains $\mathbf{u}_{\text{ext}}$ and f_{ext} on the grid points of Ω_D. One is free to chose any extension for the velocity and the right-hand side, as long as they smoothly tend to the correct values on the interface, and do not induce instabilities in the resulting flow. Given any point in the domain, a natural way to construct such an extension is to choose the value at this point to be the same as that of the closest point on the interface: this idea was first introduced in [22], and executed by following the characteristics of the signed distance function corresponding to the level set function. An equivalent formulation is to solve the equation $\nabla W \cdot \nabla \Psi = 0$, where W is the quantity to be extended: this was discussed in detail in [2], along with a fast Dijkstra-like method to solve this equation. In our case, we calculate $f = \frac{1}{2}(\nabla \phi \cdot \nabla \phi) - \kappa$ on free surface nodes, and use these values together with the condition $\nabla f \cdot \nabla \Psi = 0$ to obtain f_{ext}. For the velocity components we follow the same strategy, $\nabla u \cdot \nabla \Psi = 0, \nabla v \cdot \nabla \Psi = 0$. This algorithm for extending quantities defined on the front to off the front works very well for the velocity field in the case of Eq. (26), as it maintains the signed distance function for the level sets of Ψ.

4.3. Boundary integral equations

The details of the boundary integral solution of the axisymmetric Laplace equation have been given in [15]. However, for completeness, this section will briefly review this algorithm, focusing on the aspects of the algorithm that are somewhat 'nonstandard', namely the modified Galerkin formulation and the evaluation of the surface gradient. Further details can be found in [15].

For $\Delta \phi = 0$, the interior and exterior boundary integral equations for the axisymmetric potential $\phi(r, z)$ take the form [20]

$$\phi(\hat{r}, \hat{z}) = \int_\Gamma r\left(\frac{\partial \phi}{\partial \mathbf{n}}(r, z)\mathscr{G}(\hat{r}, \hat{z}; r, z) - \phi(r, z)\frac{\partial \mathscr{G}}{\partial \mathbf{n}}(\hat{r}, \hat{z}; r, z)\right) d\Gamma, \qquad (43)$$

$$0 = \int_\Gamma r\left(\frac{\partial \phi}{\partial \mathbf{n}}(r, z)\mathscr{G}(\hat{r}, \hat{z}; r, z) - \phi(r, z)\frac{\partial \mathscr{G}}{\partial \mathbf{n}}(\hat{r}, \hat{z}; r, z)\right) d\Gamma,$$

where the Green's function $\mathscr{G}(\hat{r}, \hat{z}; r, z)$ will be defined below. As above, the coordinates are the standard cylindrical (r, θ, z), with the θ coordinate having been integrated out. In the first equation, $(\hat{r}, \hat{z})$ is a point *interior* to the domain, in the second $(\hat{r}, \hat{z})$ lies outside, and the boundary integration is with respect to $\{r, z\}$. With an appropriate definition of the singular integrals [14], the equations are valid for $(\hat{r}, \hat{z}) \in \Gamma$, and are in fact identical. We keep both forms at this point for the subsequent discussion of the gradient.

The axisymmetric Green's function $\mathscr{G}(\hat{r}, \hat{z}; r, z)$ and its normal derivative are given in terms of the complete elliptic integrals of the first and second kind, $K(m)$ and $E(m)$,

$$\mathscr{G}(\hat{r}, \hat{z}; r, z) = \frac{1}{\pi}\frac{1}{(a + b)^{1/2}}K(m), \qquad (44)$$

$$\frac{\partial \mathscr{G}}{\partial \mathbf{n}}(\hat{r}, \hat{z}; r, z) = \frac{1}{\pi}\left[\frac{n_r}{2r(a + b)^{1/2}}\{E(m) - K(m)\} - \frac{\mathbf{n} \bullet \mathbf{R}}{(a - b)(a + b)^{1/2}}E(m)\right]. \qquad (45)$$

Here $a = r^2 + \hat{r}^2 + \Delta z^2$, $b = 2r\hat{r}$, $\Delta r = r - \hat{r}$, $\Delta z = z - \hat{z}$, $\mathbf{R} = (\Delta r, \Delta z)$ and $\mathbf{n} = \mathbf{n}(r, z)$ is the unit outward normal at the field point. Adopting the notation in [23],

$$K(m) = \int_0^{\pi/2} \frac{\mathrm{d}\theta}{(1 - m\sin^2(\theta))^{1/2}}, \tag{46}$$

$$E(m) = \int_0^{\pi/2} (1 - m\sin^2(\theta))^{1/2}\mathrm{d}\theta,$$

where the parameter m and its complementary parameter $m_1 = 1 - m$ are defined by

$$m = \frac{2b}{a+b} = \frac{4r\hat{r}}{(r+\hat{r})^2 + \Delta z^2},$$

$$m_1 = \frac{a-b}{a+b} = \frac{\Delta r^2 + \Delta z^2}{(r+\hat{r})^2 + \Delta z^2}. \tag{47}$$

The formula for the normal derivative of $\mathscr{G}$ can be derived by using the relations [39]

$$\frac{\mathrm{d}}{\mathrm{d}k}\widetilde{K}(k) = \frac{\widetilde{E}(k)}{k(1-k^2)} - \frac{\widetilde{K}(k)}{k}, \tag{48}$$

$$\frac{\mathrm{d}}{\mathrm{d}k}\widetilde{E}(k) = \frac{\widetilde{E}(k) - \widetilde{K}(k)}{k},$$

where $\widetilde{K}(k) = K(k^2)$ and $\widetilde{E}(k) = E(k^2)$.

For computations, $E(m)$ and $K(m)$ are conveniently approximated by the polynomial expansions developed by Hastings [17],

$$K(m) \approx \sum_{\nu=0}^4 a_\nu m_1^\nu - \log(m_1)\sum_{\nu=0}^4 b_\nu m_1^\nu, \tag{49}$$

$$E(m) \approx 1 + \sum_{\nu=1}^4 c_\nu m_1^\nu - \log(m_1)\sum_{\nu=1}^4 d_\nu m_1^\nu,$$

the error in these formulas being less than 2×10^{-8}; the coefficients $\{a_\nu, b_\nu, c_\nu, d_\nu\}$ can be found in [23]. Note that $\mathscr{G}$ and its normal derivative have logarithmic singularities for $(\hat{r}, \hat{z}) \to (r, z)(m_1 = 1 - m = 0)$, and consequently appropriate techniques must be employed for handling these weak singularities [15].

It is important to note that the singular behavior of the kernel functions is different at the symmetry axis: from the integration of θ, $\mathscr{G}(\hat{r}, \hat{z}; r, z)$ represents the potential due to a ring source at $\{\hat{r}, \hat{z}\}$, while on the axis this degenerates to a point. The term $a + b = r^2 + \hat{r}^2 + \Delta z^2$ that appears in the denominator in Eqs. (44) and (45) is equal to 0 on the axis, $r = \hat{r} = \Delta z = 0$. This difficulty will be circumvented by employing a Galerkin approximation with the Galerkin weight functions modified to be zero on the symmetry axis.

4.3.1. Galerkin approximation

In the following, the singular integrals will be defined as a limit to the boundary [14], and to simplify the notation, we employ $Q = (r, z)$ and $P = (\hat{r}, \hat{z})$. For convenience, the *exterior limit* form of Eq. (43) will be employed, and can be written as

$$\mathscr{P}(P) \equiv \lim_{\epsilon \to 0^+} \int_\Gamma r\left(\frac{\partial\phi}{\partial\mathbf{n}}(Q)\mathscr{G}(P_\epsilon, Q) - \phi(Q)\frac{\partial\mathscr{G}}{\partial\mathbf{n}}(P_\epsilon, Q)\right)\mathrm{d}\Gamma_Q = 0, \tag{50}$$

where $P_\epsilon = (\hat{r}_\epsilon, \hat{z}_\epsilon) = (\hat{r}, \hat{z}) + \epsilon\mathbf{N}, \mathbf{N} = \mathbf{N}(P)$ being the unit outward normal at $P = (\hat{r}, \hat{z})$.

In Galerkin, Eq. (50) is enforced 'on average' by employing a second boundary integration with respect to P,

$$0 = \int_\Gamma \hat{\psi}_k(P)\mathscr{P}(P)\mathrm{d}\Gamma_P. \tag{51}$$

The Galerkin weight function $\hat{\psi}_k(P)$ is *usually* composed of all shape functions $\psi_l(P)$ that are nonzero at a particular node P_k; in particular, this implies $\hat{\psi}_k(P_k) = 1$. In this work, a simple linear interpolation is employed to approximate the boundary and the boundary functions, and thus the Galerkin weights are piecewise linear.

To regain the symmetry (thereby allowing a symmetric-Galerkin formulation), and to ameliorate the axis singularity, the obvious course of action is to take the standard weight functions $\hat{\psi}_k(P)$ and multiply by $\hat{r}$. Thus, the equations to be solved take the form

$$0 = \lim_{\epsilon \to 0^+} \int_\Gamma \hat{r}\hat{\psi}_k(P)\int_\Gamma r\left(\frac{\partial\phi}{\partial\mathbf{n}}(Q)\mathscr{G}(P_\epsilon, Q) - \phi(Q)\frac{\partial\mathscr{G}}{\partial\mathbf{n}}(P_\epsilon, Q)\right)\mathrm{d}Q\mathrm{d}P. \tag{52}$$

4.3.2. Gradient evaluation

For the Rayleigh–Taylor problem, and moving boundary problems in general, the evaluation of the surface gradient $\nabla\phi$ is critical: this function is the surface velocity, and it enters into the equation for the free surface boundary condition. A wide

variety of boundary integral methods have been developed for gradient evaluation, see [41] for an overview. The approach employed herein [16] exploits the representation of the gradient as a boundary integral, but it will turn out that only *local* integrations (as opposed to a complete boundary integral) are required.

The surface gradient equations are obtained by differentiating, with respect to $\hat{r}$ and $\hat{z}$, the interior and exterior limit potential equations, Eq. (43), resulting in

$$\frac{\partial}{\partial \mathscr{X}}\phi(P) = \int_\Gamma r\left(\frac{\partial\phi}{\partial\mathbf{n}}(Q)\frac{\partial\mathscr{G}}{\partial\mathscr{X}}(P_\epsilon,Q) - \phi(Q)\frac{\partial^2\mathscr{G}}{\partial\mathscr{X}\partial\mathbf{n}}(P_\epsilon,Q)\right)dQ, \tag{53}$$

$$0 = \int_\Gamma r\left(\frac{\partial\phi}{\partial\mathbf{n}}(Q)\frac{\partial\mathscr{G}}{\partial\mathscr{X}}(P_\epsilon,Q) - \phi(Q)\frac{\partial^2\mathscr{G}}{\partial\mathscr{X}\partial\mathbf{n}}(P_\epsilon,Q)\right)dQ, \tag{54}$$

where $\mathscr{X}$ is either $\hat{r}$ or $\hat{z}$ and the interior $\epsilon \to 0^-$ and exterior $\epsilon \to 0^+$ limits are understood. Expressions for the kernel functions can be obtained by using Eq. (48), and are listed in [15].

Unlike the limit equations for surface potential, wherein the jump term in the integral of $\partial\mathscr{G}/\partial\mathbf{n}$ ensures that the boundary equations are identical, the two gradient boundary equations are in fact distinct. The key idea is therefore to take the difference of Eqs. (53) and (54), as then all nonsingular integrals will immediately cancel in the limit. In Galerkin form, once again employing the modified weight functions, this 'limit-difference' equation takes the form

$$\int_\Gamma \hat{r}\hat{\psi}_k(P)\frac{\partial}{\partial\mathscr{X}}\phi(P)d\Gamma = \left\{\lim_{\epsilon\to 0^-} - \lim_{\epsilon\to 0^+}\right\}, \tag{55}$$

$$\int_\Gamma \hat{r}\hat{\psi}_k \int_\Gamma r\left(\frac{\partial\phi}{\partial\mathbf{n}}(Q)\frac{\partial\mathscr{G}}{\partial\mathscr{X}}(P_\epsilon,Q) - \phi(Q)\frac{\partial^2\mathscr{G}}{\partial\mathscr{X}\partial\mathbf{n}}(P_\epsilon,Q)\right)dQdP.$$

Moreover, for the axisymmetric analysis, note that the weakly singular log terms, arising from the elliptic integrals $K(m)$ and $E(m)$, do not appear in the gradient evaluation. The elliptic integrals in fact appear solely through the $E(1) = 1$ contribution, and as a consequence, the integrations can be carried out entirely analytically. This provides an extra measure of accuracy, as no numerical quadratures are involved. As noted above, the computational work is also drastically reduced: the double Galerkin integration over the complete boundary is replaced by just the singular integrations.

For the numerical implementation of both the potential, Eq. (43), and gradient equations, Eq. (55), the main task is the evaluation of singular integrals. The discussion of the singular integration algorithms can be found in [15].

4.4. Regridding of the free surface

In a level set formulation the position of the front is only known implicitly through the nodal values of the level set function Ψ. In order to extract the front, an interpolation (*e.g.* first or second order) of the Ψ data on the grid points can be constructed (for example, see [7] as well as [34] for information about reinitialization strategies). Here we use a first order linear approximation of the free surface, yielding a polygonal interface formed by unevenly distributed nodes, termed LS nodes. As a result of this extraction technique, two LS nodes can lie very close together, and this can cause difficulties and instabilities for the boundary element calculation. To overcome this problem, and also to achieve more front resolution when needed, a front node regridding technique has been employed.

In this scheme, an initialization point on the front is selected according to a particular criterion, such as minimum neck radius, velocity modulus, or front curvature. This point divides pieces of the front in two halves and new nodes are chosen so that, lying in the same polygon, they are redistributed by arclength according to the formula:

$$s_{i+1} - s_i = d_0(1 + s_i(f_0 - 1)),$$

where s_i denotes the arclength distance from node i to the initialization point ($i = 0$) and d_0, f_0 are user selected parameters. These regridded nodes on the front are used to create the input file for the BEM calculations and are termed BEM nodes.

4.5. The algorithm

To initialize the front position and the front velocity potential we use the Rayleigh–Taylor analytical solution for the liquid column. If the initial configuration is a closed drop, the initial potential and velocity will be set to zero and motion is started by the initial front curvature.

The basic algorithm can be summarized as follows:

1. Initialize $\Gamma_0(s), \Phi(s,0), \mathbf{u}, f$.
2. Initialize the level set function Ψ on Ω_D.
3. Initialize G by extending $\Phi(s,0)$ onto grid points of Ω_D.
4. Extend $\mathbf{u}$ and f off the front onto Ω_D.
5. Update G using (27) in Ω_D.
6. Move the front with velocity $\mathbf{u}$ using (26) in Ω_D.

7. Bicubic interpolate G from grid points of Ω_D to the front nodes to obtain new boundary conditions for (25).
8. Generate $\Omega(t)$ and solve (25), using the Boundary Element Method, to obtain the velocity $\mathbf{u}$ on the front nodes.
9. Calculate curvature κ and the source term f on the front nodes. Go back to step 4 and repeat forward in time.

A more detailed algorithm including regridding is:

Initialization of $\Gamma_0(s), \Phi^0, G^0, \Psi^0$ and f^0.
do k=1, max_time_steps
- Extend u, v, f from initial LS front nodes (and reinitialize Ψ and G if needed).
- Evolve the front updating Ψ and the potential updating G.
- Find number of fronts and LS nodes on each front.

do i=1, number_of_fronts
- Redistribute LS nodes to find BEM nodes for the ith front.
- Compute curvature κ on BEM nodes for the ith front.
- Bicubic-interpolate G on BEM nodes to find the potential for the ith front.
- Generate $\partial\Omega_i(t_n)$ for the ith front.
- Calculate u, v on BEM nodes for the ith front solving (25).
- Find f on BEM nodes for the ith front.
- Store u, v, f of the ith front in a packed array.
- Rename BEM nodes as LS nodes for the next extension.
end do
end do

5. Numerical results

To study the convergence properties of this method and its ability to simulate the Rayleigh–Taylor (R–T) instability and subsequent drop formation, we first present numerical results corresponding to the linearized model; this allows a comparison of the computed and analytical solutions for short times. Next, we show the numerical experiments performed for the fully nonlinear model before and after pinch-off time. Finally, we study the self-similar (scaling) behavior of the minimum neck radius, the corresponding axial coordinate, and the velocity near pinch-off.

5.1. The linearized model

To compare computed results with the R–T analytical solution we perturb the front with a cosine wave of amplitude $\epsilon = 0.001$ and wave number $k = 0.697$, which corresponds to the maximum growth rate. We simulate one wave period, thus

Table 1
Discrete L_2 norms of the listed variables for $\Delta r = 0.01$.

Case	Δt	r_f	ϕ	u	v	ϵ_r
(a)	0.01	4.92e−07	1.65e−06	2.08e−05	4.19e−05	3.3e−03
(b)	0.001	2.36e−07	6.99e−07	9.49e−06	1.59e−05	1.6e−03

Table 2
Discrete L_2 norms of the listed variables for $\Delta t = 0.01$.

Case	Δr	r_f	ϕ	u	v	ϵ_r
(c)	0.5	4.90e−05	7.39e−04	5.10e−04	1.70e−04	6.2e−02
(d)	0.05	5.82e−07	2.32e−06	2.76e−05	6.11e−05	2.1e−03
(e)	0.005	4.92e−07	1.65e−06	2.08e−05	6.19e−05	1.9e−03

Table 3
Pinching characteristics.

Case	t_p	z_p
(a)	22.2753	1.33
(b)	22.2843	1.29
(c)	22.2704	1.33

the length of the cylinder is $L_2 = 9$ and the initial radius is $r_0 = 1$. Let $\Omega_D = [-3, 3] \times [0, 9]$ be the fixed domain that contains the free boundary for all $t \in [1, 1.5]$, $\Delta r = \Delta z$ the grid size and Δt the time step. We denote by Δs the arclength spacing between BEM nodes. We have run a series of numerical tests to study the convergence properties of the computed solution
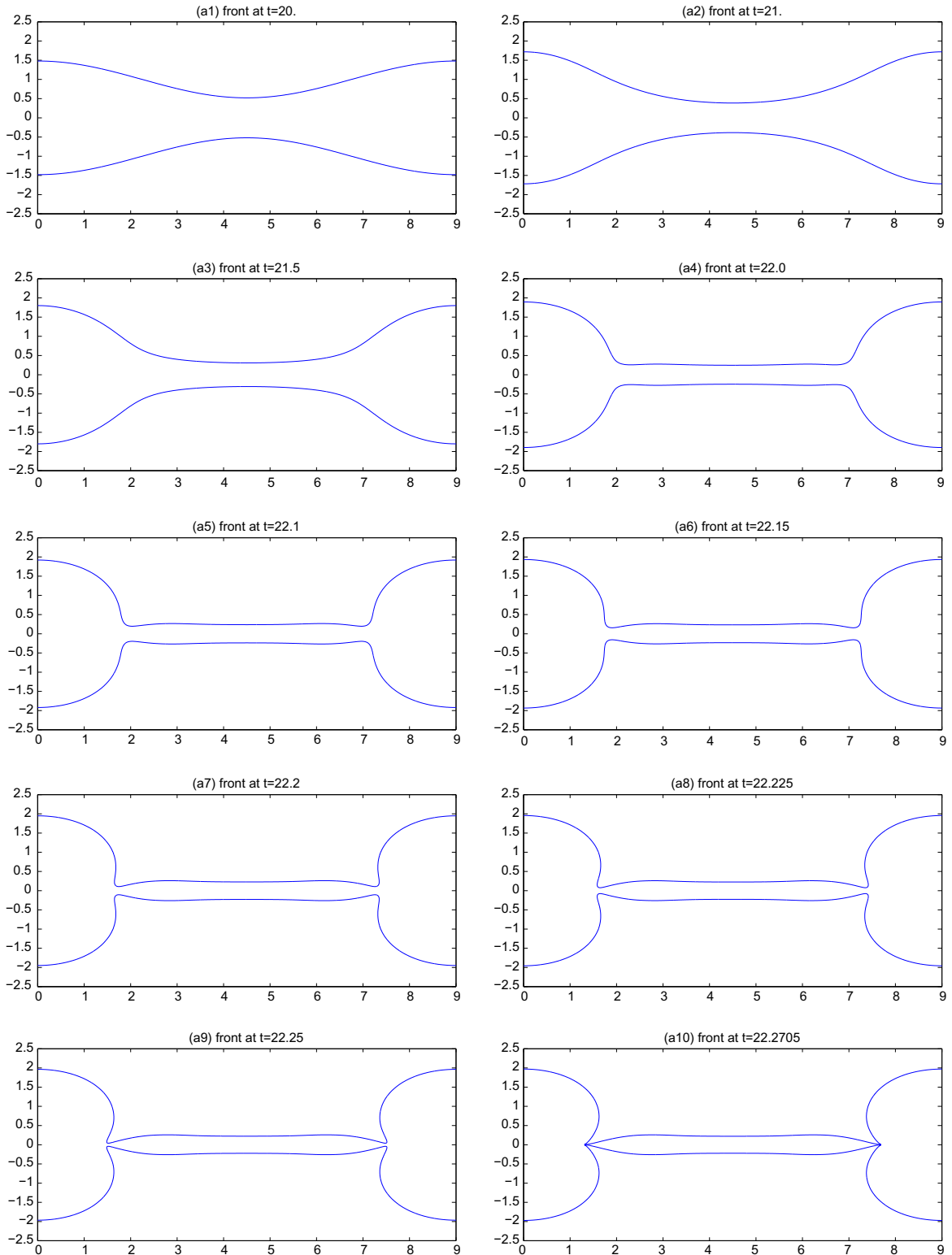

Fig. 5. Front profiles at indicated times.

with respect the analytical solution. The discrete L_2 norm (at BEM nodes) of the difference has been calculated at each time step for each of the variables, namely the front position, r_f, the velocity potential, ϕ, the axial velocity, u, and the radial velocity, v. In Table 1 we show the discrete norms at $t = 1.5$ for the listed variables, with fixed $\Delta r = 0.01$ and various Δt. We note here that for $\Delta t = 0.1$ instabilities grow and the solution blows up before $t = 1.5$. In Table 2 we show same discrete norms, this time with $\Delta t = 0.01$ and varying Δr. The discrete L_2 norm of the relative error in the front position is almost equal to the absolute error norm, due to $r_f \approx 1$. Nevertheless, as the wave amplitude is very small it is valuable to check how the L_2 discrete norm of the relative error in the wave amplitude, ϵ_r, changes with respect the discretization parameters. This is shown in the last column of Tables 1 and 2.

From these results it can be seen that we achieve a convergence rate with time that is roughly first order: some of the variations may have to do with the interpolations and regridding involved. With respect to the grid spacing, Δr, the discrete norms also decrease, but it is not so obvious that we achieve first order convergence looking at cases (d) and (e). This can be due to the fact that the front profile is almost flat and more space resolution does not increase accuracy. Conservation of
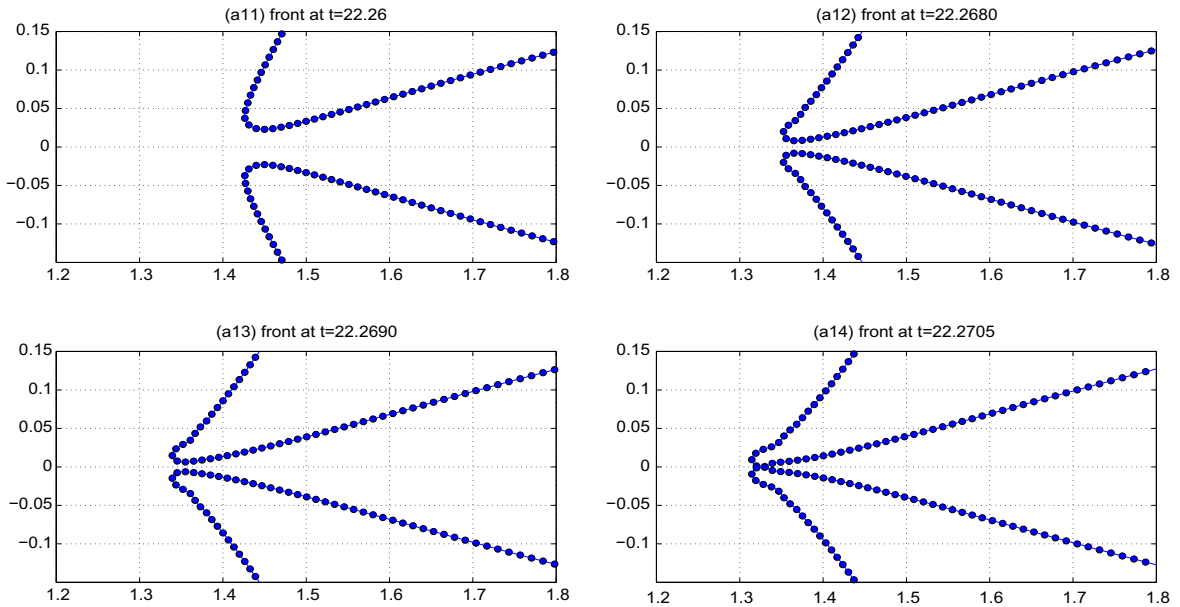
Fig. 6. Front profiles and BEM nodes near pinch-off time.
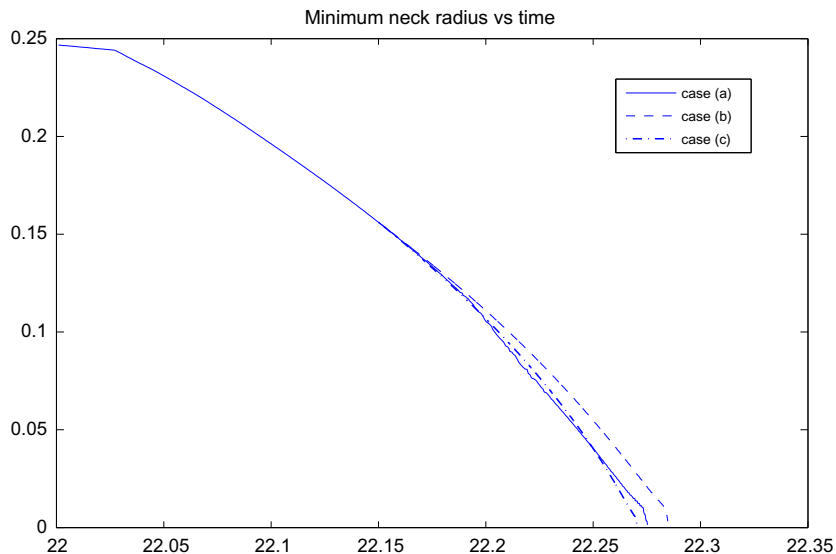
Fig. 7. Minimum neck radius from $t = 22.15$ to pinch-off time for all cases.

volume has also been checked, giving all cases a value of $|V - V_c| < 10^{-6}$ for all times, except for case (c). This is coherent with the fact that the front position, r_f, has always a precision of 10^{-7} for those cases. All these numerical tests have been run with 91 BEM nodes. Runs for 181 BEM nodes have also been undertaken, given almost the same numerical results and we do not show the corresponding tables. We now continue the problem beyond the range of the linearized assumptions which leads to the fully nonlinear potential flow model.

5.2. The full nonlinear model

Next we present the numerical experiments performed for the full nonlinear potential flow model. The physical configuration and computational domain is the same as before. Variables are initialized from the analytical solution at $t = 20$.
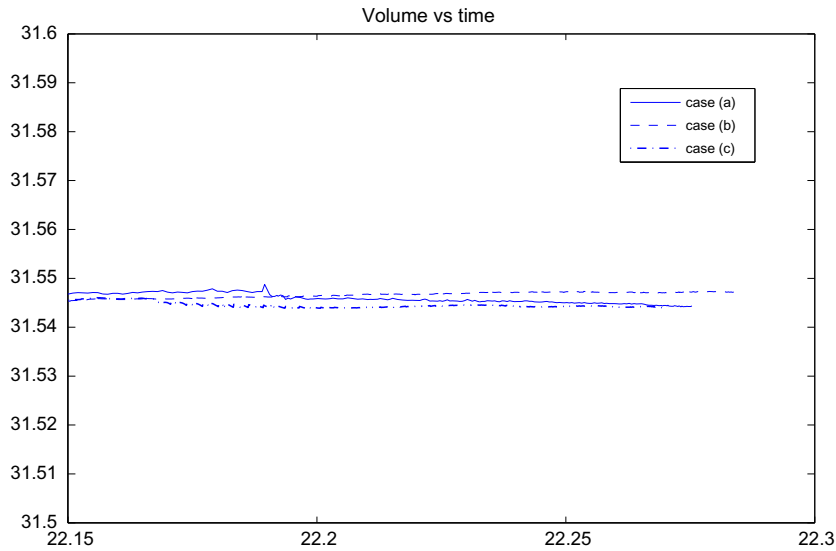
Fig. 8. Volume from t = 22.15 to pinch-off time for all cases.
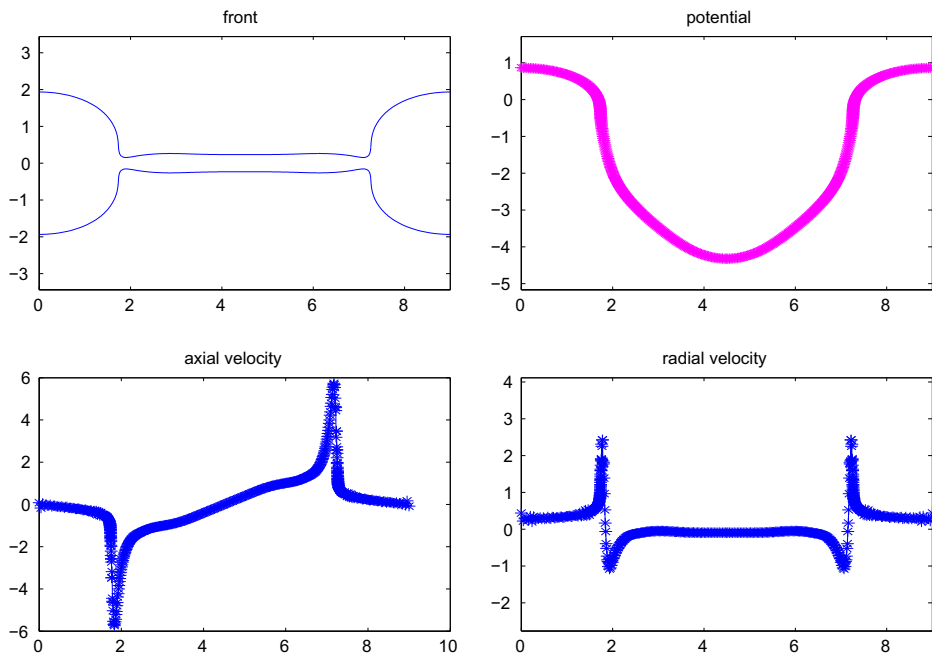
Fig. 9. Variables at BEM nodes for t = 22.15.

Before first pinch-off, and at each time step, a set of new BEM nodes will be selected according to the regridding algorithm. The front position is also symmetric with respect $z = L_2/2$, thus we divide the front in two halves. The LS node in $[0, L_2/2]$ corresponding to r_{min} will be the starting point for the regridding. Nodes in $[L_2/2, L_2]$ will be copied using the left to right symmetry. This procedure will give a variable free boundary spacing Δs. After first pinch-off, the BEM nodes will be taken equally spaced in arclength for each separate drop. The fixed domain Ω_D mesh size $\Delta r = \Delta z$ has to be small enough
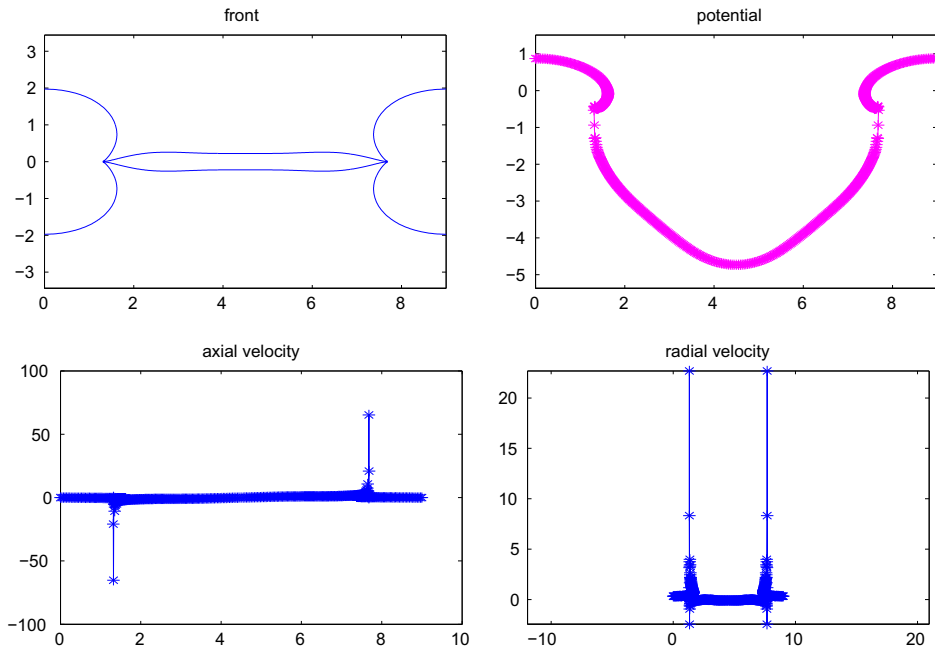
Fig. 10. Variables at BEM nodes for $t = 22.2705$.
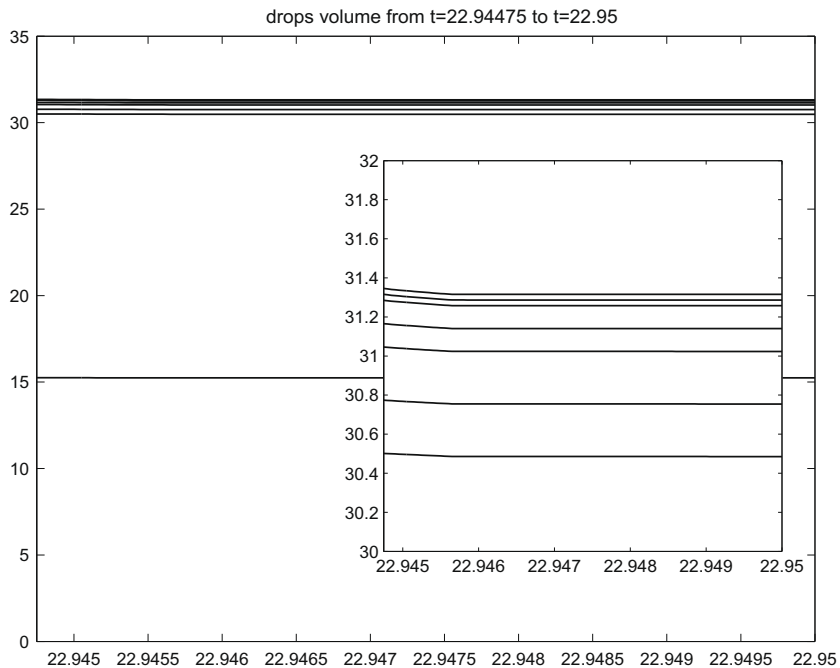
Fig. 11. Accumulated drops volume from $t = 22.94475$ to $t = 22.95$.
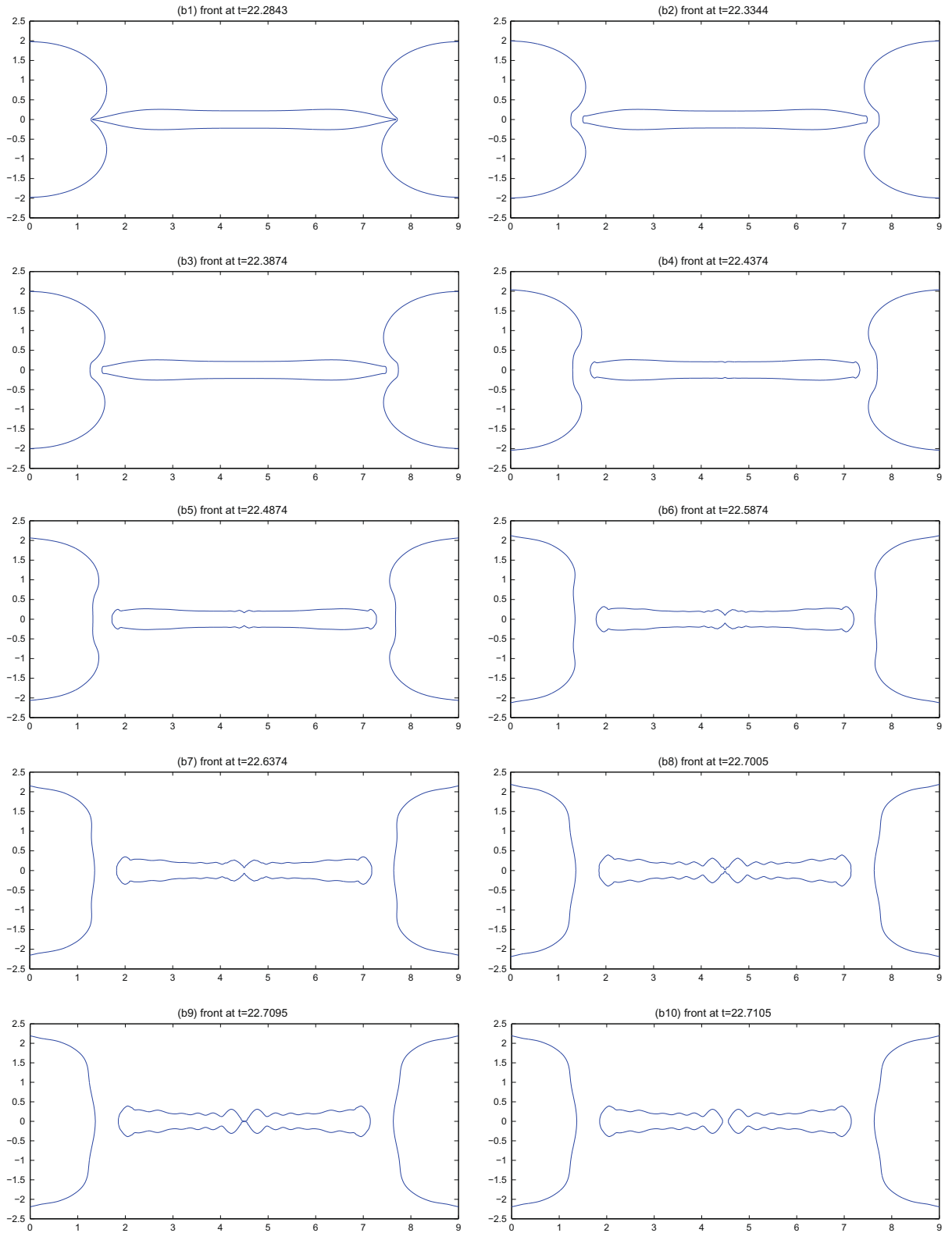
Fig. 12. Front profiles after pinch of at various times.
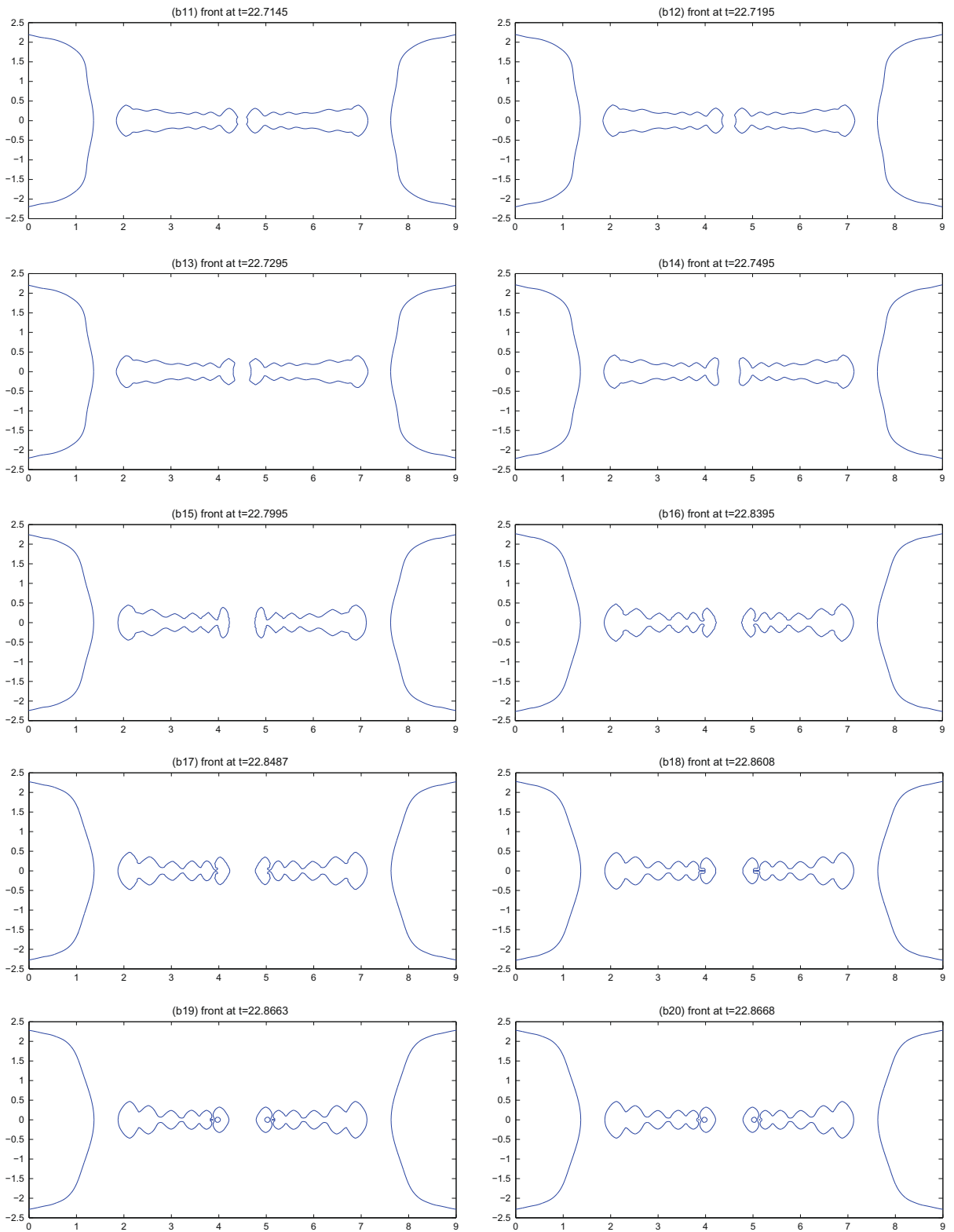
Fig. 12 (*continued*)
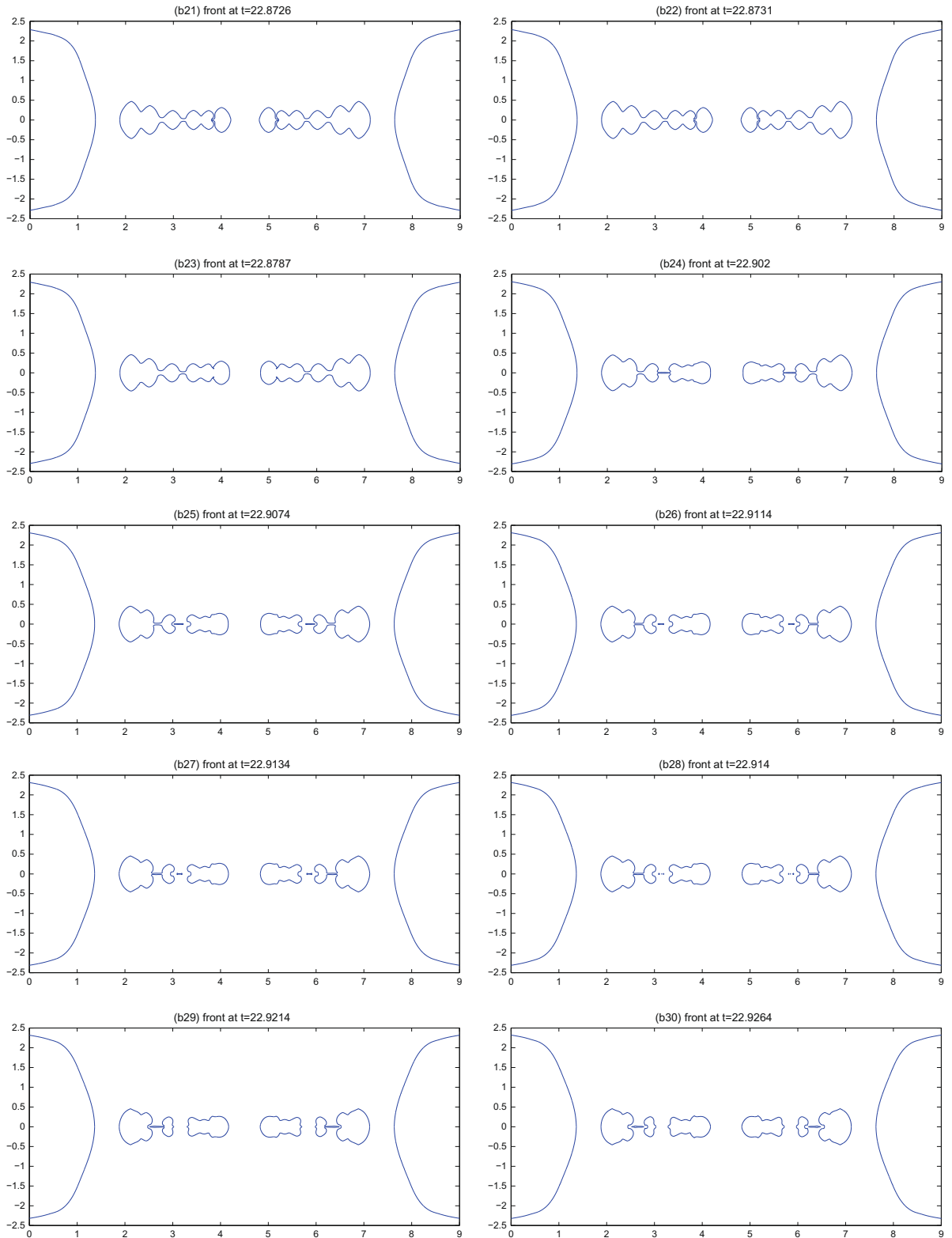
Fig. 12 (*continued*)

to achieve good space resolution for Eqs. (40) and (41), the zero level set node representation, the extensions and the variables bicubic interpolation from grid nodes to front BEM nodes. The time step cannot remain constant during the whole
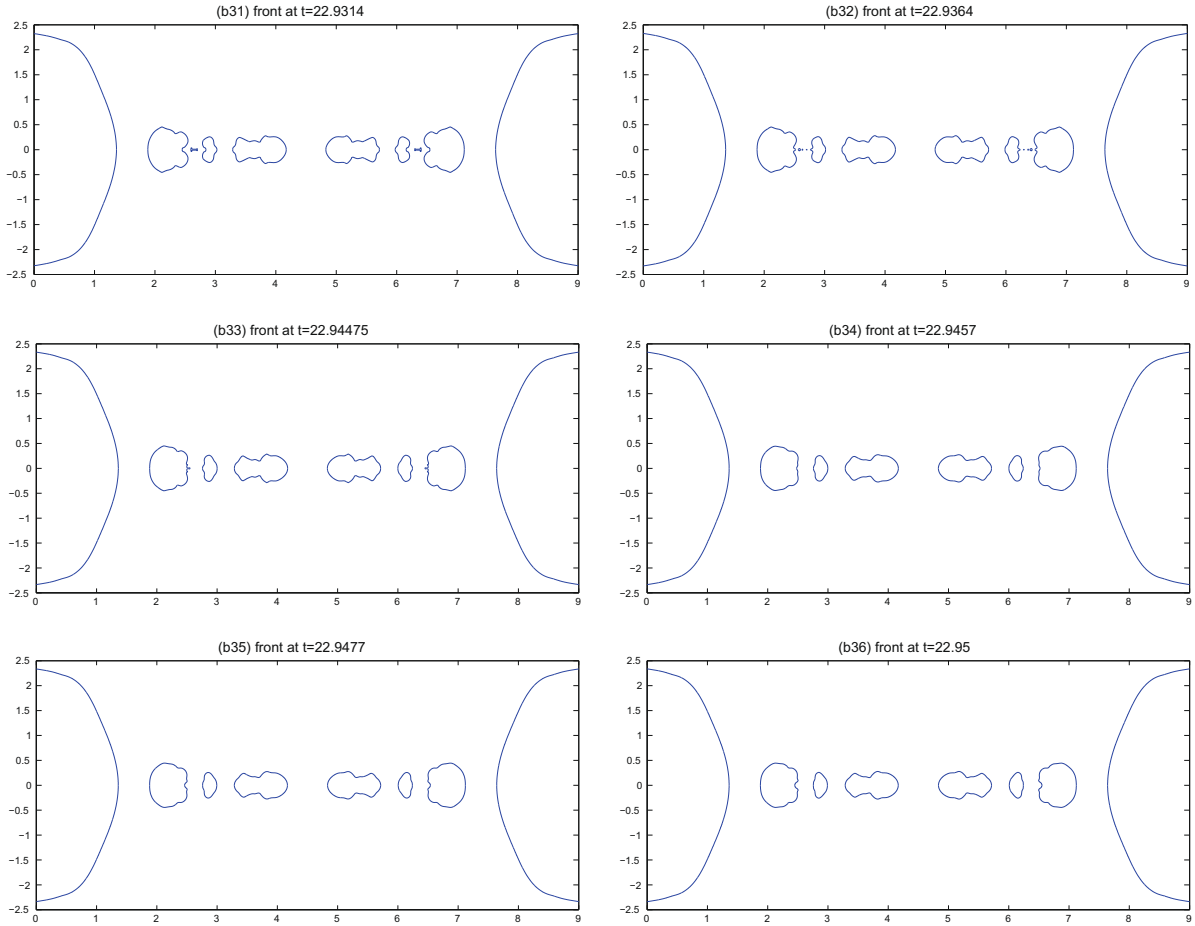
Fig. 12 (*continued*)

computation. It has to be selected at each time through a stability criterion. For our explicit schemes it is selected to fulfill the CFL condition and so as to resolve small amplitude capillary waves that can appear on the front. The chosen criterion is

$$\Delta t \leqslant \min \left(\frac{\Delta r}{|\mathbf{u}|_{\max}}, 0.2 \Delta s_{\min}^{3/2} \right)$$

In the absence of a nonlinear analytical solution, the computed behavior will be checked by examining, with respect the discretization parameters, several key flow characteristics: the evolution of the total volume, V_c, minimum neck radius, $r_{\min}$, the pinch-off time t_p and the axial coordinate at pinch-off, z_p.

5.2.1. Results before pinching

From $t = 20$ to $t = 22$ the solution does not change too rapidly with time and the discretization parameters employed are: $\Delta r = 0.01$, $\Delta s = 0.1$, $f_0 = 1$ and a fixed time step $\Delta t = 0.001$. From $t = 22$ to pinch-off time the flow accelerates and the following cases have been studied:

(a) $\Delta r = 0.01$; $\Delta s = 0.02$, $f_0 = 2$, $\Delta t = 0.001$ initially.
(b) $\Delta r = 0.01$; $\Delta s = 0.01$, $f_0 = 2$, $\Delta t = 0.0001$ fixed.
(c) $\Delta r = 0.005$; $\Delta s = 0.01$, $f_0 = 2$, $\Delta t = 0.0001$ initially.

The computed pinch-off time, t_p, and axial coordinate, z_p are displayed in Table 3.

Discrepancies in t_p and z_p for case (b) with respect to case (a) and (c) are due to the fixed time step, an adaptive time step appears to be a better strategy. Nevertheless, front profiles are almost the same for all cases. Profiles for case (c) are shown in Fig. 5 at selected times, and in Fig. 6 zoomed fronts showing overturning and BEM nodes near pinch-off are also presented. In Figs. 7 and 8 the evolution of the cylinder volume and minimum neck radius with time are presented for all cases. Finally, in Figs. 9 and 10 the main variables are shown for $t = 22.15$ and $t = 22.2705$: The front position, the velocity potential at the

front nodes, and the axial and radial velocities respectively. Reinitialization of the level set function or the velocity potential has not been performed before pinching.

5.2.2. Results after pinching

For the numerical experiments after pinch-off, two different flow periods have been considered. From $t = 22.2704$ to $t = 22.8486$, the tube collapses first into 3 drops and then at $t_p = 22.7095$ the central drop breaks into two separate drops at $z_p = 4.5$. The discretization parameters used are: $\Delta r = 0.01$, $\Delta s \approx 0.04$ (for the lateral drops), $\Delta s \approx 0.03$ (for the central drop) and a fixed time step $\Delta t = 0.0001$.

Regarding the last flow period, from $t = 22.8487$ to $t = 22.9501$, the two central drops evolve very quickly and develop complicated structures, due to capillary waves; meanwhile the flow on the lateral drops slows down. The discretization parameters used are: $\Delta r = 0.01$, $\Delta s \approx 0.03$ (for the lateral drops), $\Delta s = 0.02$ (for all the central drops), $\Delta s = 0.01$ for tiny drops with total arclength less than 0.2 and a fixed time step $\Delta t = 0.0001$. For this lapse of time and to check the validity of the
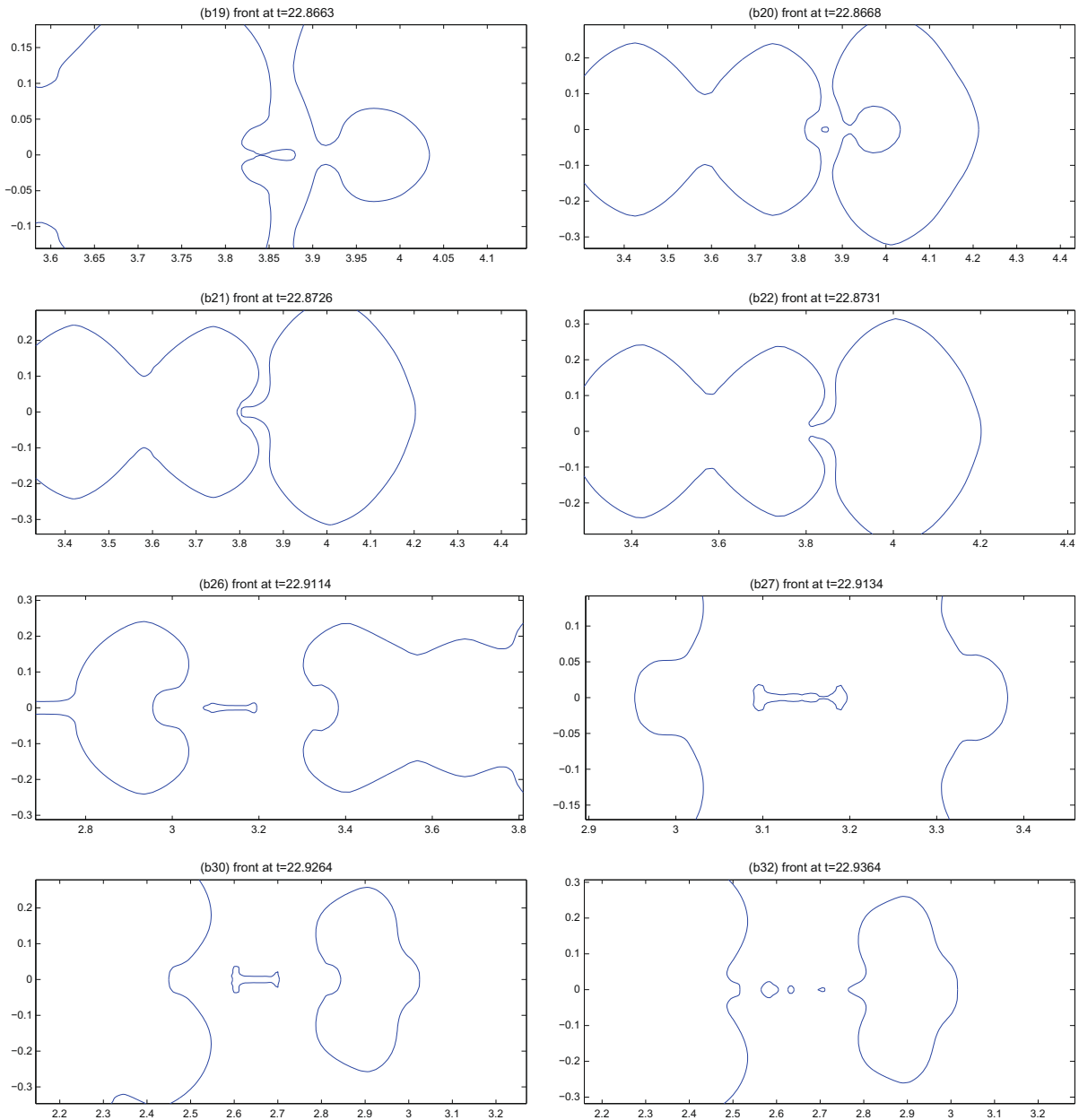
Fig. 13. Zoomed figures at selected times.

results, we have run the same previous case with the smaller mesh size $\Delta r = 0.005$. The time step has been adjusted according to the stability criteria, which gives a minimum value of $\Delta t = 10^{-5}$ at the end of the simulation. A cascade of pinch-off events and a reconnection occurs, obtaining basically the same results for both values of the mesh size. Subsequent pinch-off events occur within 2×10^{-3} time units of difference between both mesh sizes. Obviously, the finer grid gives more resolution of the front shape and very tiny structures appear which were not present in the coarser grid. This is illustrated in Fig. 14, which shows a detail of the front profile obtained with both mesh sizes, marking the location of BEM nodes and LS nodes. In Fig. 15 we focus on the shape of one satellite droplet at the end of the simulation, in order to show that drop roughness holds under refinement.
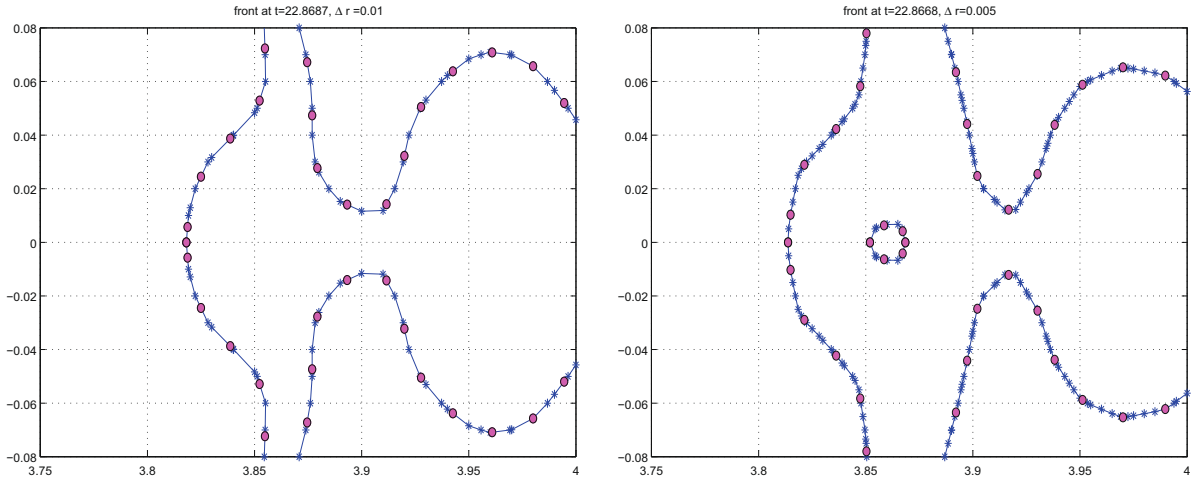
Fig. 14. BEM and LS nodes at $t = 22.8687$ with $\Delta r = 0.01$ (left) and BEM and LS nodes at $t = 22.8668$ with $\Delta r = 0.005$ (right). BEM ($\bigcirc$), LS ($*$).
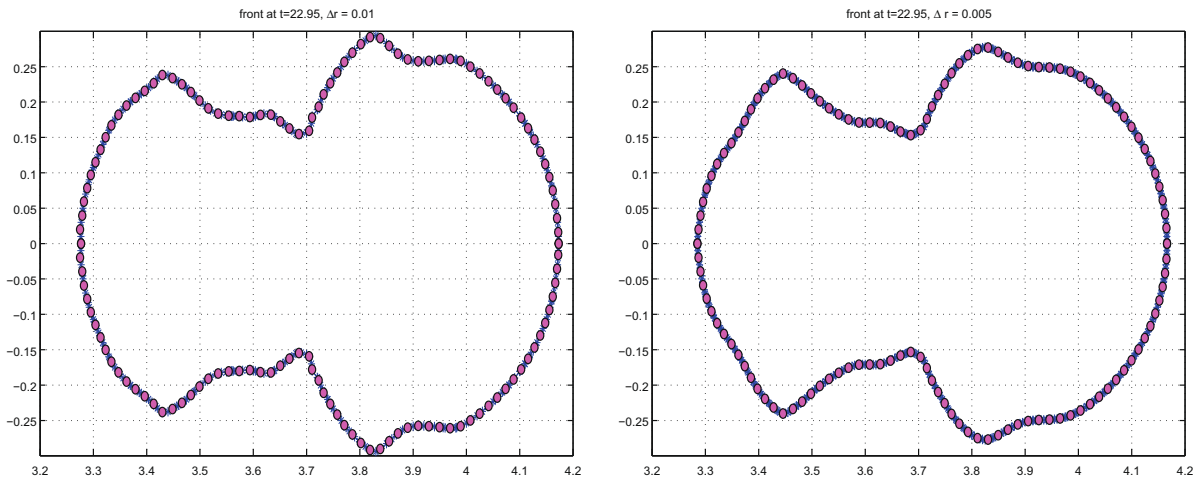
Fig. 15. BEM and LS nodes at $t = 22.95$ with $\Delta r = 0.01$ (left) and BEM and LS nodes at $t = 22.95$ with $\Delta r = 0.005$. BEM ($\bigcirc$), LS ($*$).
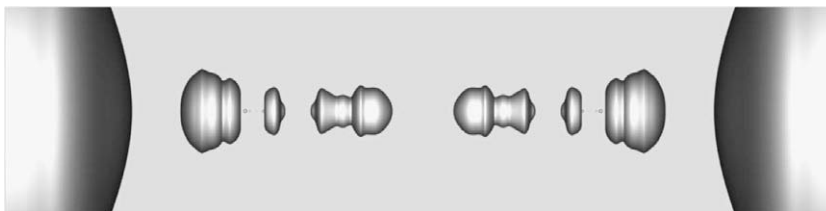

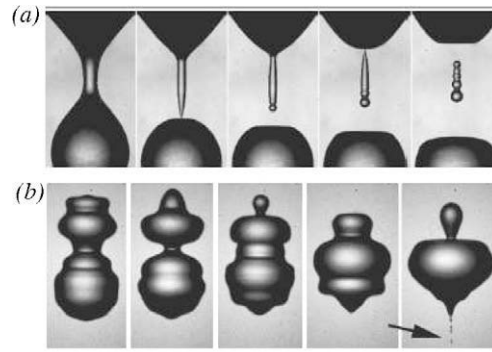**Fig. 16.** 3D rendering of computed results at $t = 22.9364$.

Figure 2: (a) Satellite formation during the pinch-off of a drop from a 5 mm nozzle. (b) Sequence shows the ejection of 30 mm micro-droplets which emerge at 10 m/s.

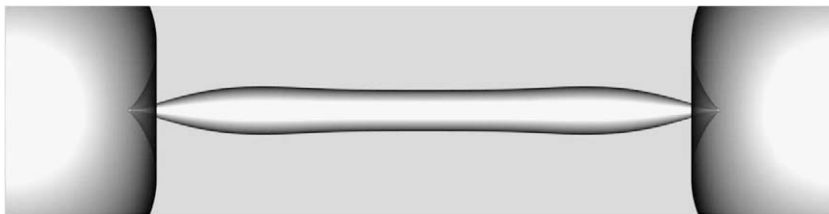**Fig. 17.** Laboratory photos of a water satellite drop taken from [37].

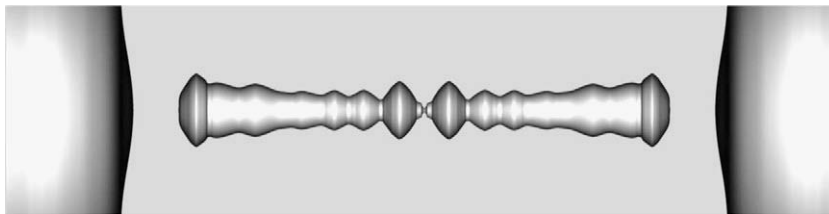
Fig. 18. 3D rendering of computed results at t = 22.2704.

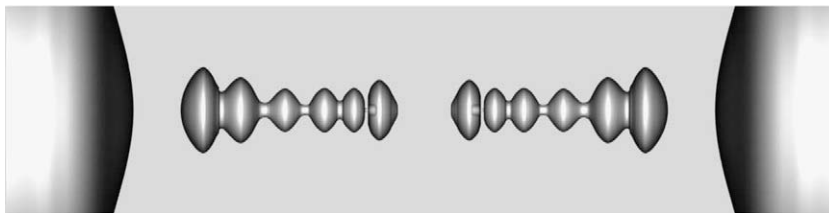**Fig. 19.** 3D rendering of computed results at t = 22.7095.

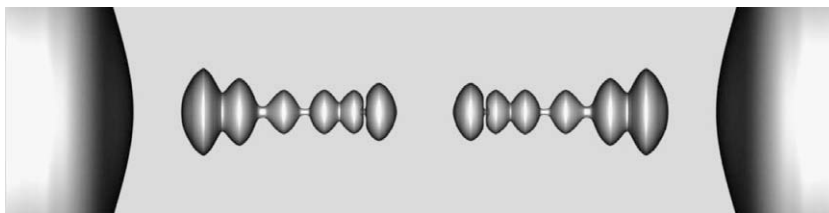**Fig. 20.** 3D rendering of computed results at t = 22.8608.

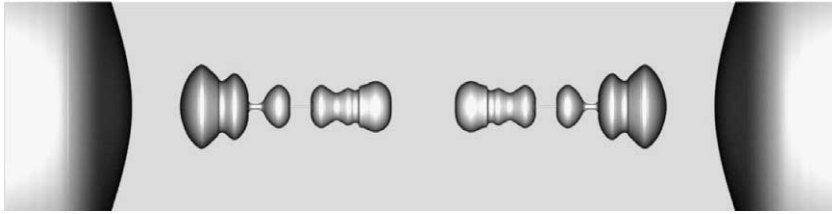**Fig. 21.** 3D rendering of computed results at t = 22.8731.

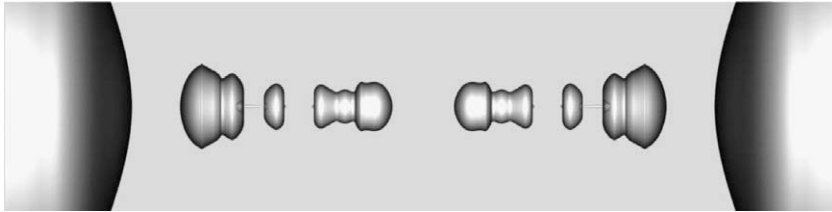**Fig. 22.** 3D rendering of computed results at t = 22.902.

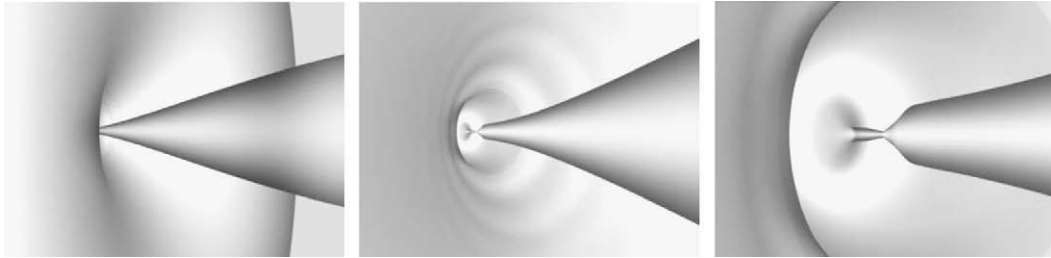**Fig. 23.** 3D rendering of computed results at t = 22.9214.

Fig. 24. 3D details of first pinch-off at t = 22.2704.

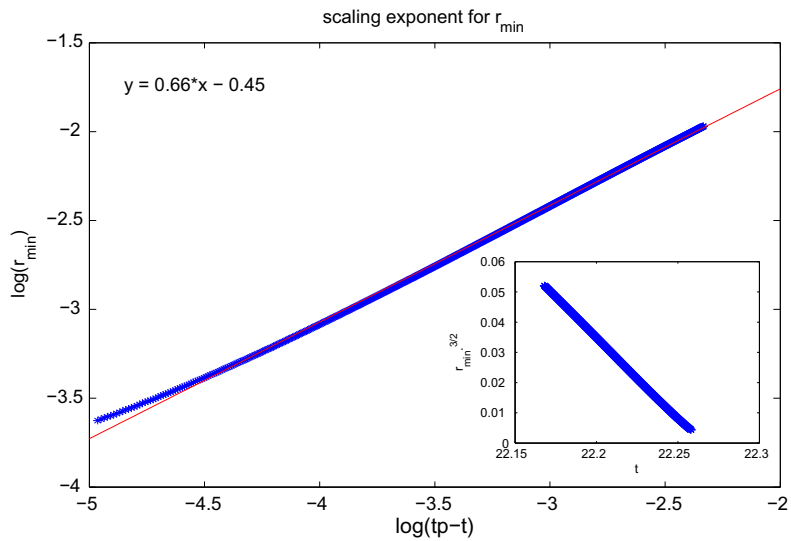**Fig. 25.** Scaling exponent for r_{min}.

Reinitialization of the level set function Ψ, and the potential function, G, was only performed when needed, approximately every 250 time steps. As the reinitialization algorithm is only first order accurate some small amount of volume is lost in each reinitialization. The very tiny drops with a volume less than 10^{-4} are not well resolved in this calculation and
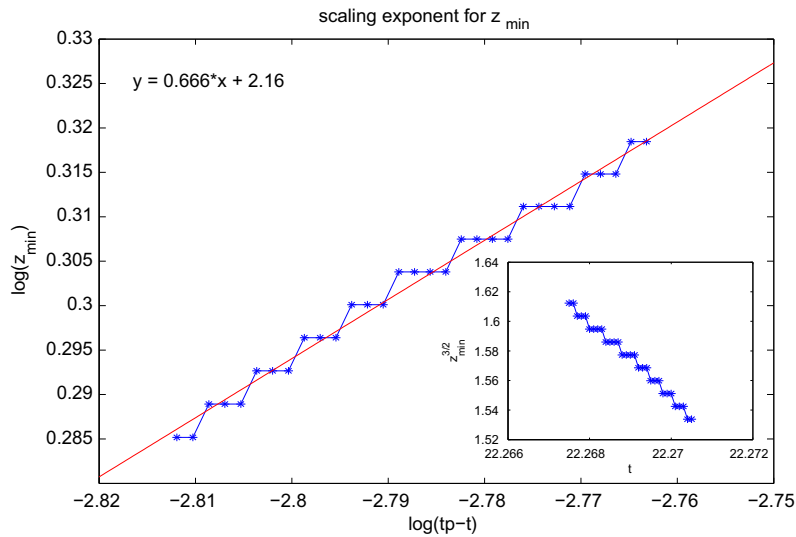
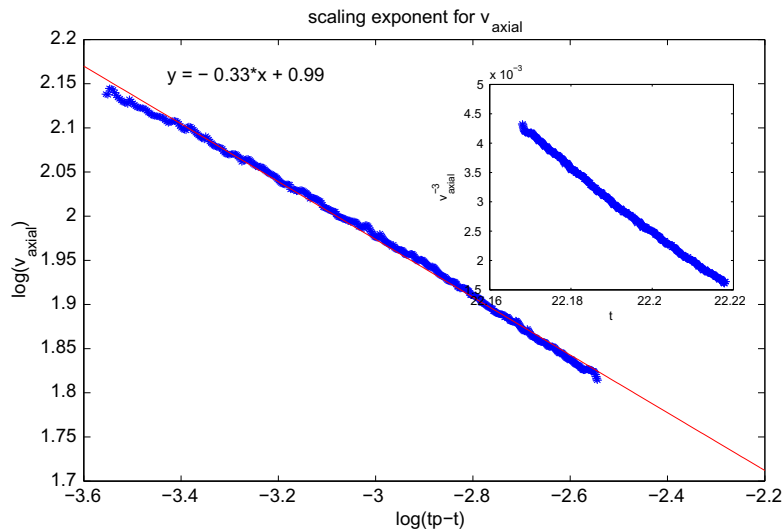**Fig. 26.** Scaling exponent for $z_{\min}$.

Fig. 27. Scaling exponent for v_{axial}.

they tend to loose volume. These are artificially removed from the calculation when the drop size is less than $\Delta r/2$. In Table 5 we show the times at which there is a change in the number of drops and, for each time, the volume distribution between drops. The evolution of the accumulated drops volume at the end of the simulation, from t=22.94475 to t=22.95, is depicted in Fig. 11. In this figure the volume of each drop is plotted above the previous one, in order to show the contribution of each drop to the total volume. We have used two different volume axes to capture the volume contribution of the satellite drops. The volume of the lateral drops is very well conserved, whereas some volume is lost in the evolution of the satellite drop. This is due to reinitialization and removement of the very tiny structures. Nevertheless the total volume lost after pinch-off is only 0.7%.

In Fig. 12 we show the front profiles corresponding to the finer grid at various times. In Fig. 13 a zoom of some outstanding events corresponding to jet ejection or tiny satellites breaking in three very small drops is also presented. To support the numerical results, we include in Fig. 16 a 3D rendering of the computed profiles at $t = 22.9364$ and in Fig. 17 real water satellite drops taken from [37]. Note the resemblance between computed versus real satellite drop shapes. In Figs. 18–23, 3D renderings of the computed front profiles at (or near) main pinching events are also included. For these renderings a transparent skin has been used to see structures which otherwise would be hidden. Finally, in Fig. 24, we have progressively focused on the first pinch-off time with different camera angles.
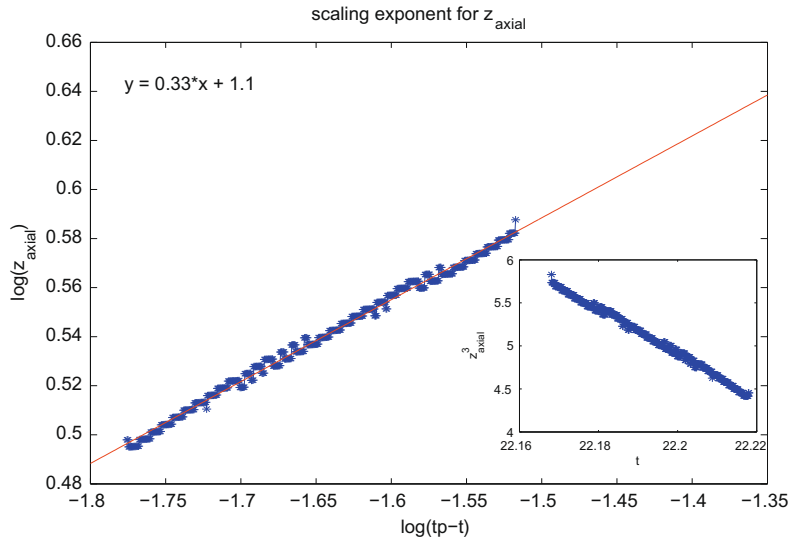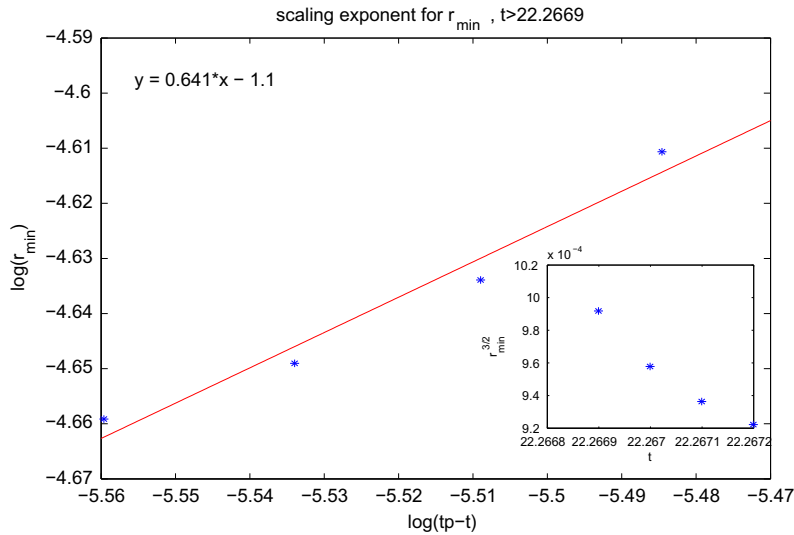
Fig. 28. Scaling exponent for z_{axial}.

Fig. 29. Scaling exponent for r_{min}, $t > 22.2669$.

Table 4
Satellite drop pinching characteristics.

t_p	z_p	r_{min} exp.	z_{min} exp.
22.7095	4.5	0.678	
22.8608	3.965	0.679	
22.9022	3.288	0.695	0.663
22.9210	2.4997	0.667	0.63

5.3. Self-similar pinch-off scalings

From dimensional analysis and assuming the behavior near pinch-off is locally determined and independent of initial conditions, it has been shown in [9,19], that the solution in the pinch-off region is self-similar as $\tau = t_p - t \rightarrow 0$, where τ is the time until pinch-off. Since the velocity potential is harmonic, ($\Delta\phi = 0$), it follows that r and z scales are likely to be
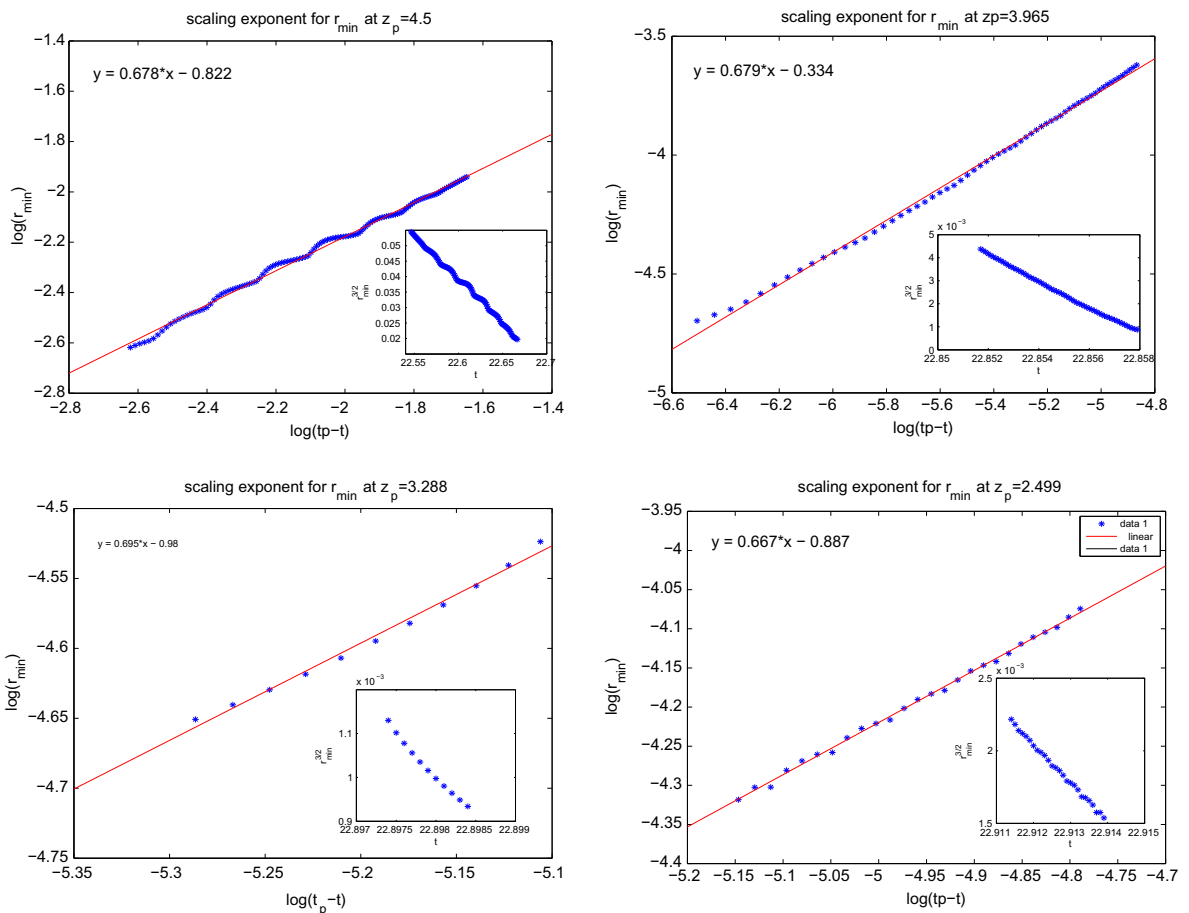
comparable as pinch-off is approached. Balancing inertial and surface tension forces and using the dimensionless variables (14) we arrive at the similarity scalings:

$$r \sim z \sim \left(\frac{\gamma}{\rho}\right)^{\frac{1}{3}} \tau^{\frac{2}{3}}, \quad \phi \sim \left(\frac{\gamma}{\rho}\right)^{\frac{2}{3}} \tau^{\frac{1}{3}}, \quad u \sim \left(\frac{\gamma}{\rho}\right)^{\frac{1}{3}} \tau^{-\frac{1}{3}}. \tag{56}$$

Table 5
Drops volume distribution for main time events, $t_1 = 22.2843$, $t_2 = 22.7095$, $t_3 = 22.8609$, $t_4 = 22.8668$, $t_5 = 22.8726$, $t_6 = 22.9022$, $t_7 = 22.9074$, $t_8 = 22.9140$, $t_9 = 22.9210$, $t_{10} = 22.9364$, $t_{11} = 22.9450$.

t_1	t_2	t_3	t_4	t_5	t_6	t_7	t_8	t_9	t_{10}	t_{11}
15.3180	15.3180	15.2751	15.2735	15.2713	15.2610	15.2596	15.2575	15.2558	15.2524	15.2426
15.3180	15.3180	15.2751	15.2735	15.2713	15.2610	15.2596	15.2575	15.2558	15.2524	15.2426
0.9058	0.4529	0.3883	0.3876	0.4525	0.3064	0.3063	0.3059	0.2747	0.2732	0.2691
	0.4529	0.3883	0.3876	0.4525	0.3064	0.3063	0.3059	0.2747	0.2732	0.2691
		0.0660	0.0656		0.1218	0.1214	0.1206	0.1202	0.1197	0.1172
		0.0660	0.0656		0.1218	0.1214	0.1206	0.1202	0.1197	0.1172
			2.6e−6			4.1e−5	1.e−5	0.0317	0.0307	0.0289
			2.6e−6			4.1e−5	1.e−5	0.0317	0.0307	0.0289
							3.7e−6		3.4e−5	
							3.7e−6		3.4e−5	
							6.1e−7		3.1e−6	
							6.1e−7		3.1e−6	
									8.5e−7	
									8.5e−7	

Fig. 30. Scaling exponents for $r_{\min}$ at indicated pinching locations.
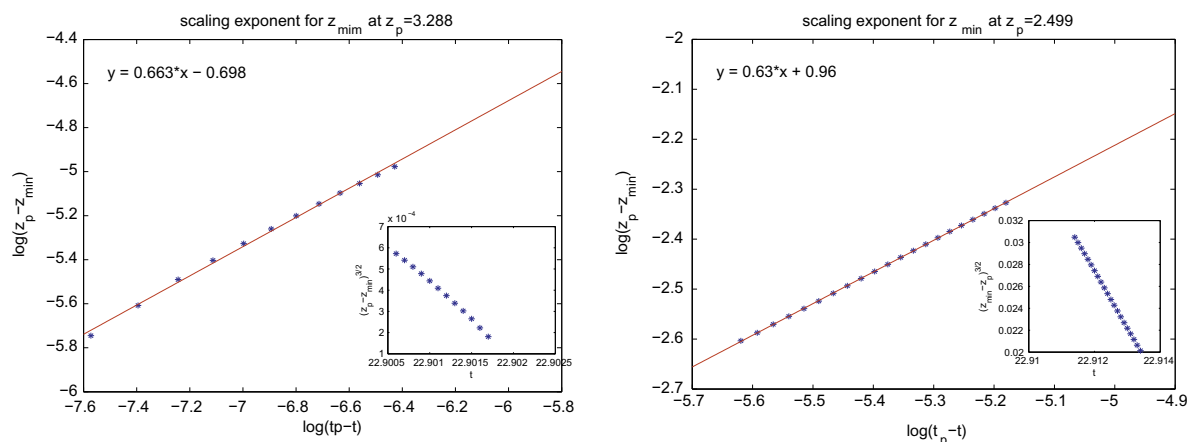
Fig. 31. Scaling exponents for z_{min} at indicated pinching locations.

To check if the computed variables behave according to the above power scaling laws near pinch-off, we plot r_{min} versus time. A straight line is obtained from which we extrapolate the value of t_p. Then a linear fit to the log–log plot of r_{min} versus τ will give us the scaling exponent. In Fig. 25 we show the above mentioned straight lines, and the MatLab linear fit gives an exponent value of 0.66, in very good agreement with the predicted value of 2/3. Exactly the same procedure is undertaken with z_{min}, and as shown in Fig. 26 an exponent of 0.666 is obtained. For the velocity scaling we search for the maximum axial velocity near the point (r_{min}, z_{min}) for each time and name z_{axial} the axial coordinate at which this maximum, v_{axial}, occurs. We found for v_{axial} an exponent value of -0.33 and for z_{axial} a value of 0.33, as shown in Figs. 27 and 28.

We note that for $0 < r_{min} < 0.0095$ the scaling exponents obtained are not in very good agreement with theoretical value, with a 4% relative error, see Fig. 29. This can be due to the acceleration of the flow, and more space and time resolution could be needed. However, the z_{min} exponent remains in very good agreement with theory up to pinch-off time.

The satellite drop formed after first pinch-off time pinches again at its middle point $z_p = 4.5$ at $t_p = 22.7096$. It evolves smoothly at the beginning but as soon as a neck is formed at $z = 4.5$ capillary waves seem to appear at this point. These waves propagate through the surface of the drop creating crests and valleys which are the structures observed in laboratory experiments. Subsequent pinch-off and reconnection occurs in the left and right satellite drops, sometimes with small jet ejection or new tiny satellite drop formation, see Fig. 13.

The scaling exponents of the secondary pinch-off events have also been analyzed. In Table 4 we present the events that have been studied with the corresponding scalings exponents for r_{min} and z_{min}. The procedure to obtain these exponents is the same as explained above and we show the plotted data in Figs. 30 and 31. Note that when overturn does not occur during pinching, the scaling law for z_{min} does not apply.

6. Conclusion

To summarize, in this paper we have presented a complete Eulerian description of a 3D axisymmetric potential flow model for a single fluid, with a moving boundary that undergoes topological changes. A coupled level set-boundary integral algorithm has been developed for this case and applied to the numerical approximation of non-viscous pinch-off, corresponding to the most unstable Rayleigh mode. Numerical results and convergence tests show that even first order level set schemes can reproduce the complicated satellite drop structures observed in laboratory experiments. To further verify the validity of the numerical results we have shown that the self-similar scaling exponents for all pinch-off events are in accordance with the theoretical ones.

Acknowledgments

References

[1] D. Adalsteinsson, J.A. Sethian, A fast level set method for propagating interfaces, J. Comput. Phys. 118 (2) (1995) 269–277.
[2] D. Adalsteinsson, J.A. Sethian, The fast construction of extension velocities in level set methods, J. Comput. Phys. 148 (1999) 2–22.
[3] D. Adalsteinsson, J.A. Sethian, Transport and diffusion of material quantities on propagating interfaces via level set methods, J. Comput. Phys. 185 (1) (2002) 271–288.

 [4] B. Ambravaneswaran, E.D. Wilkes, O.A. Basaran, Drop formation from a capillary tube: comparison of one-dimensional and two-dimensional analysis and occurrence of satellite drops, Phys. Fluids 14 (2002) 2606.
 [5] Y.J. Chen, P.H. Steen, Dynamics of inviscid capillary breakup: collapse and pinchoff of a film bridge, J. Fluid Mech. 341 (1997) 245–267.
 [6] A.U. Chen, P.K. Notz, O.A. Basaran, Computational and experimental analysis of pinch-off and scaling, Phys. Rev. Lett. 88 (2002) 174501.
 [7] D.L. Chopp, Some improvements of the fast marching method, SIAM J. Sci. Comput. 23 (2001) 230–244.
 [8] G. Colicchio, M. Greco, O.M. Faltinsen, A BEM-level set domain-decomposition strategy for non-linear and fragmented interfacial flows and multiphase materials, Int. J. Numer. Methods Eng. 67 (2006) 1385–1419.
 [9] R.D. Day, E.J. Hinch, J.R. Lister, Self-similar capillary pinchoff of an inviscid fluid, Phys. Rev. Lett. 80 (1998) 704–707.
[10] J. Eggers, Nonlinear dynamics and breakup of free-surface flows, Rev. Mod. Phys. 69 (3) (1997) 865–929.
[11] J. Eggers, E. Villermaux, Physics of liquid jets, Rep. Prog. Phys. 71 (2008) 036601.
[12] M. Garzon, D. Adalsteinsson, L.J. Gray, J.A. Sethian, A coupled level set-boundary integral method for moving boundaries simulations, Interf. Free Bound. 7 (2005) 277–302.
[13] M. Garzon, J.A. Sethian, Wave breaking over sloping beaches using a coupled boundary integral-level set method, Int. Ser. Numer. Methods 154 (2006) 189–198.
[14] L.J. Gray, Evaluation of singular and hypersingular Galerkin boundary integrals: direct limits and symbolic computation, in: V. Sladek, J. Sladek (Eds.), Singular Integrals in the Boundary Element Method, Computational Mechanics Publishers, 1998, pp. 33–84 (Chapter 2).
[15] L.J. Gray, M. Garzon, V. Mantič, E. Graciani, Galerkin boundary integral analysis for the axisymmetric Laplace equation, Int. J. Numer. Methods Eng. 66 (2006) 2014–2034.
[16] L.J. Gray, A.V. Phan, T. Kaplan, Boundary integral evaluation of surface derivatives, SIAM J. Sci. Comput. 26 (1) (2004) 294–312.
[17] C. Hastings, Approximations for Digital Computers, Princeton University Press, Princeton, 1995.
[18] J.B. Keller, M.J. Miksis, Surface tension driven flows, SIAM J. Appl. Math. 43 (1983) 268–277.
[19] D. Leppinen, J.R. Lister, Capillary pinch-off in inviscid fluids, Phys. Fluids 15 (2003) 568–578.
[20] J.A. Liggett, L.F. Liu, The Boundary Integral Equation Method for Porous Media Flow, Allen and Unwin, London, 1983.
[21] S.P. Lin, Breakup of Liquid Sheets and Jets, Cambridge University Press, 2003.
[22] R. Malladi, J.A. Sethian, B.C. Vemuri, Shape modeling with front propagation: a level set approach, IEEE Trans. Pattern Anal. Mach. Intell. 17 (2) (1995) 158–175.
[23] L.M. Milne-Thompson, in: M. Abromowitz, I.A. Stegun, Elliptic Integrals, Handbook of Mathematical Functions, National Bureau of Standards, Washington, DC, 1972, pp. 587–626 (Chapter 17).
[24] Patrick K. Notz, Osman A. Basaran, Dynamics of drop formation in an electric field, J. Colloid Interf. Sci. 213 (1999) 218–237.
[25] S. Osher, J.A. Sethian, Fronts propagating with curvature-dependent speed: algorithms based on Hamilton–Jacobi formulations, J. Comput. Phys. 79 (1988) 12–49.
[26] J. Plateau, Experimental and theoretical researches on the figures of a liquid mass withdrawn from the action of gravity, in: Annual report of The Board of Regents of the Smithsonian Institution, Washington, DC, 1863, pp. 270–283.
[27] L. Rayleigh, On the instability of jets, Proc. Lond. Math. Soc. 10 (1879) 4.
[28] F. Savart, Memoire sur la constitution des veines liquides lancees par des orifices circulaires em mince paroi, Ann. Chim. 53 (1833) 337.
[29] R.M.S.M. Schulkes, The evolution and bifurcation of pendant drops, J. Fluid Mech. 278 (1994) 83–100.
[30] J.A. Sethian, J. Strain, Crystal growth and dendrite solidification, J. Comput. Phys. 98 (1992) 231–253.
[31] Sethian, J.A., An Analysis of Flame Propagation, Ph.D. Dissertation, Dept. of Mathematics, University of California, Berkeley, CA, 1982.
[32] J.A. Sethian, Curvature and the evolution of fronts, Commun. Math. Phys. 101 (1985) 487–499.
[33] J.A. Sethian, Numerical methods for propagating fronts, in: P. Concus, R. Finn (Eds.), Variational Methods for Free Surface Interfaces, Springer-Verlag, NY, 1987.
[34] J.A. Sethian, A fast marching level set method for monotonically advancing fronts, Proc. Nat. Acad. Sci. 93 (4) (1996) 1591–1595.
[35] J.A. Sethian, Level Set Methods and Fast Marching Methods, Cambridge Monographs on Applied and Computational Mathematics, Cambridge University Press, 1999.
[36] J.A. Sethian, P. Smereka, Level set methods for fluid interfaces, Annu. Rev. Fluid Mech. 35 (2003) 341–372.
[37] S.T. Thoroddsen, Micro-droplets and micro-bubbles imaging motion at small scales, Nus. Eng. Res. News 22 (1) (2007).
[38] A. VanderWyst, A. Christlieb, M. Sussman, I.D. Boyd, Simulation of liquid metal droplets from field emission, Commun. Comput. Phys. 2 (2007) 640–661.
[39] E.T. Whittaker, G.N. Watson, A Course of Modern Analysis, Cambridge University Press, Cambridge, 2002.
[40] J.-D. Yu, S. Sakai, J.A. Sethian, A coupled level set projection method applied to ink jet simulation, Interf. Free Bound. 5 (4) (2003) 459–482.
[41] Zhiye Y. Zhao, Shengrui Lan, Boundary stress calculation – a comparison study, Comput. Struct. 71 (1999) 77–85.